The final publication is available at

https://doi.org/10.1016/j.memsci.2011.05.016

Additional Information

Fluid Dynamic Modeling of Oxygen Permeation through Mixed Ionic-Electronic Conducting Membranes

J. M. Gozálvez-Zafrilla[1], A. Santafé-Moros[1], S. Escolástico[2], J. M. Serra[2,*]

[1]*Chemical and Nuclear Engineering Depart. Universidad Politécnica de Valencia, C/Camino de Vera s/n 46022 Valencia (Spain)*

[2]*Instituto de Tecnología Química (Universidad Politécnica de Valencia - Consejo Superior de Investigaciones Científicas). Av. de los Naranjos s/n.Valencia, Spain. 46022.*

Abstract

The oxygen transport in a lab-scale experimental set-up for permeation testing of oxygen transport membranes has been modeled using computational fluid dynamics using Finite Element Analysis. The modeling considered gas hydrodynamics and oxygen diffusion in the gas phase and vacancy diffusion of oxygen in a perovskite disc-shaped membrane at 1273 K. In a first step, the model allowed obtaining the coefficient diffusion of oxygen. The parametric study showed that the set-up geometry and flow rate in the air compartment did not have major influence in the oxygen transport. However, very important polarization effects in the sweep-gas (argon) compartment were identified. The highest oxygen permeation flux and the lowest oxygen concentration on the membrane surface were obtained for the following conditions (in increasing order of importance): (1) a large gas inlet radius; (2) short gas inlet distance; and (3) a high gas flow rate.

Keywords: CFD; oxygen permeation; perovskite; membrane; oxygen transport membrane; permeation setup; transport modeling

* corresponding autor. E-mail: jmserra@itq.upv.es; Fax: +34.963.877.809,

1. Introduction

High-purity oxygen production through ceramic membranes at high temperature [1] is an interesting cost-effective alternative to the cryogenic methods for several industrial applications. Membrane separation will make possible to reduce energy requirements and investment costs. Among the different applications, the use in fossil fuel power plants in the so-called *Oxyfuel* process [2,3] would allow minimizing CO_2 emissions since the final flue gas stream consists principally of moist CO_2, which can be readily liquefied and transported. In this case, the ceramic oxygen transport membrane modules can be thermally integrated and make possible to match the desired oxygen production due to the intrinsic modularity of these systems. Apart from usual applications of oxygen in several industries, e.g. steel industry or petrochemistry, oxygen transport membranes are able to achieve high grade purity (theoretical selectivity of 100% for defect-free membranes) extending its possible applications. Additionally, another important field of application of this kind of membranes is their implementation in high-temperature catalytic membrane reactors while typically reactions are synthesis gas production from methane [4, 5], oxidative coupling of methane to yield ethane and ethylene [6, 7, 8], pocket selective ammonia oxidation [9], among others. The high selectivity can be achieved because oxygen separation is based on the transport of oxygen-ion vacancies through the lattice of a crystalline mixed oxide material. The most usual oxygen-ion conducting materials are based on the perovskite structure (ABO_3) or related structures [5,10] and comprise Fe/Co/Ni and mixtures of lanthanide and alkali-earth metals in suitable proportions.

Fundamental research on this topic makes use of bench-scale testing units, where the oxygen permeation through a small disc-shaped membrane sample is measured as a function of different operation variables such as temperature, oxygen partial pressure at the inlet of each chamber, inlet gas flow rate in each chamber, etc. A widely used permeation set-up uses a disc membrane (15 - 25 in diameter and 0.2 to 2 mm in thickness) with the geometry shown in Figure 1. Nevertheless, the determination of the true oxygen flux through the material is not always straightforward. Indeed, there are several *lurking* experimental variables that introduce some noise/deviation to the permeation results. This is especially patent when comparing experimental data from different groups, which apparently employ similar permeation units. Among the different possible causes for this, it can be highlighted (*i*) temperature gradients in the membrane; (*ii*) oxygen partial pressure gradients on the membrane surface (at each membrane side); and (*iii*) gas transport limitations from/toward the membrane surface (polarization) which results in a reduction of the net driving force (gradient of oxygen chemical potential). The last aspect can be particularly critical for thin-supported membranes on porous substrates [11]. The

importance of these effects associated to the fluid dynamics in the testing unit depends on the chosen experimental set-up configuration and operating conditions.

Ghidossi et al. [12] made a review of computational dynamics applied to membranes, emphasizing the possible contribution of computational fluid dynamics in the development of new membrane processes. Some other studies have been devoted to the validation and the application of computational simulators to reliably predict the fluid dynamic and the separation performances in inorganic membranes modules for gas separations. Koukou et al. [13] demonstrated the validity of two-dimensional mathematical model to predict the influence of non-ideal flow effects on membrane separator performance. Furthermore, Takaba et Nakao [14] tested a CFD simulator to evaluate the influence of the concentration polarization on the membrane performance. They model a bi-channel and a tubular geometry when treating a H_2/CO mixture. These results showed that the CFD simulation is capable of evaluating the concentration polarization effect in a membrane module for gas separation and they concluded that the CFD simulation can be used to design a membrane module involving prediction of selectivity and cut. More recently, Coroneo et al. [15] used a CFD simulation without introducing any simplified hypothesis on the velocity field and the concentration distribution of the species. They obtained good agreement between the experimental and the predicted data and concluded that CFD is a useful and reliable tool for design of new membrane modules.

Siegel [16]] made a thorough review of the application of computational modeling of heat and mass transfer in polymer electrolyte membrane fuel cells where it is shown an overview of models in literature according to their dimensionality. For three-dimensional models, the modeling efforts of the fluid dynamics of the gas phase inside the cells have conducted to a more realistic approach of the cell performance. Moreover, this review evaluates the CFD available software. In particular, the potential of COMSOL Multiphysics is highlighted as an efficient tool for modeling complex systems for which fluid dynamics and mass and heat transfer are relevant. Sousa et al. [17] used COMSOL to obtain the concentration profile of the components in direct ethanol fuel cells. COMSOL and other software [18, 19] have also been used to model solid oxide fuel cells.

Oxygen diffusion has been also modeled using computational techniques in diverse industrial processes like oxyfuel combustion [20,21] or fuel rods [22]. The oxygen diffusion in ceramic membrane modules has been studied by our group [23, 24] and by others researchers [2, 25]. Recently, [26] the diffusion in porous mixed ionic-electronic layers, e.g. solid oxide fuel cell cathodes, has been modeled successfully using COMSOL, and CFD combined with impedance spectroscopy made it possible the determination of intrinsic materials properties as the diffusion coefficient.

1.1. Aim and structure of the work

In this work, it is intended to understand the effect of several experimental factors on the measured permeation rate by means of computational fluid dynamics modeling using COMSOL Multiphysics®. The aims of this contribution are (*i*) to assist the researchers in the selection of the most suitable setup configuration and operating conditions and/or to prevent the use of inadequate operating conditions/set-up geometries; and (*ii*) to calculate the intrinsic material properties by considering the real fluid dynamics in both membrane chambers.

The strategy followed in this work is the next. Firstly, flux experimental results were obtained for an experimental rig of specified geometry. This geometry is taken as a base case. Secondly, a model of the system using COMSOL Multiphysics was developed taking into account the different involved phenomena. Thirdly, a diffusion coefficient of oxygen vacancies was obtained as in intrinsic material parameter by an iterative method to match flux experimental results to those given by the model for the base case. Finally, using the vacancy diffusion coefficient obtained, the effects of changes in the inlet geometry with respect to the base case (inlet radius and distance to the membrane) and inlet gas flow rate were studied for both permeate and feed chamber.

The manuscript is organized accordingly to the mentioned procedure:

- In the experimental and methods section, the experimental set-up is described. The modeling using COMSOL Multiphysics and the procedure of determination of the vacancy diffusion coefficient for a reference case are also shown.

- The results and discussion section is organized in the following parts: study of the reference geometry with determination of the diffusion coefficient of oxygen vacancies, parametric study of the geometry of the inlet of the feed compartment, parametric study of the geometry of the

sweep-gas inlet of the permeate compartment, and parametric study of the entering flows of gas in both compartments.

2. Experimental and methodology

2.1. Experimental set-up and conditions

A detailed scheme of the experimental set-up is shown in Figure 1b. A membrane disc is placed between the feed and permeate compartments. The membrane disc has a diameter of 15 mm and thickness of 0.75 mm. The membrane material was an oxygen deficient perovskite ($La_{1-y}Sr_yFeO_{3-\delta}$ with y=0.1). Due to the necessary seal, the area exposed of the membrane is 1.039 cm^2. Dry air enters into the feed chamber from an inlet placed in the axis of the module. The flow enters perpendicularly to the membrane and then goes downwards before exiting upwards for the external annulus. The sweep-gas (argon) enters into the permeate compartment from an inlet tube placed in the vertical axis and exits through the external area upwards.

The distances (separation from the membrane surface) and diameters of the feed and sweep-gas inlet tubes of the experimental rig used are shown in Table 1. The experiments to characterize the membrane were performed at a temperature of 1000 °C and nearly atmospheric pressure (20 mbar overpressure), and using a gas flow rate of 50 cm^3(STP)/min for both air and sweep-gas feed. The sweep flow rate was also varied (50; 100; 150; 200 50 cm^3(STP)/min) in a parametric study. This set of geometry parameters and operating conditions define the *reference case* (Table 1).

2.2. Oxygen transport through ceramic membranes

The most studied ceramic membranes to selectively separate oxygen at high temperature are perovskite membranes. The generic chemical formula for a perovskite is $A_{1-y}A'_yBO_{3-\delta}$, where usually A = La; A' = Ca or Sr and B = Cr, Fe, Co, Ni or Mn.

The point defect model indicates that there is a relationship between the partial pressure of oxygen and the vacancy concentration in a structure with oxygen non-stoichiometry. The diffusion of oxygen is explained by the Wagner's theory through a mechanism that considers vacancy diffusion and the electronic transport together. There are two cases of non-stoichiometric materials: oxygen deficient perovskite and oxygen excess perovskite. For the oxygen deficient

perovskite that we used in the experiments ($La_{0.9}Sr_{0.1}FeO_{3-\delta}$), the following reactions are considered [27] using the Kroger-Vink notation:

- Defect reaction:

$$2Fe_{Fe}^{\cdot} + O_O^x \leftrightarrow 2Fe_{Fe}^x + V_O^{\cdot\cdot} + \tfrac{1}{2}O_2\ (g)$$
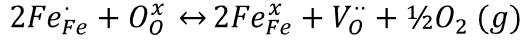
- Disproportionation reaction:
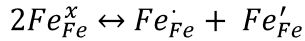
$$2Fe_{Fe}^x \leftrightarrow Fe_{Fe}^{\cdot} + Fe_{Fe}'$$

where $Fe_{Fe}^{\cdot}$ and Fe_{Fe}' are a Fe^{+4} or Fe^{+2}, respectively, formed in a Fe^{+3} position, and $V_O^{\cdot\cdot}$ is an oxygen vacancy.

For these reactions, we have the following equilibrium constants:

$$K_2 = \frac{[Fe_{Fe}^x]\cdot[V_O^{\cdot\cdot}]\cdot p_{O2}^{\frac{1}{2}}}{[Fe_{Fe}^{\cdot}]^2\cdot[O_O^x]} \tag{1}$$

$$K_2 = \frac{[Fe_{Fe}^{\cdot}]\cdot[Fe_{Fe}']}{[Fe_{Fe}^x]^2} \tag{2}$$

These equations can be combined with the electroneutrality condition and mass balances for the species that suffer disproportionation to obtain an equilibrium relationship between oxygen pressure in the gas and vacancy concentration in the solid. As the calculation is rather time-consuming, the vacancy concentrations were previously calculated for a number of pressures to create an interpolation function. To do so, the following values of equilibrium constants at 1000 °C obtained by van Hassel et al. [27] were used: $K_2 = 7\cdot10^{-2}$ atm$^{1/2}$ and $K_3 = 1\cdot10^{-6}$. Figure 2 shows the equilibrium calculated with these constants.

2.3. Modeling

The concentration gradients through the membrane obtained by simulation are of great interest to determine the local diffusion coefficient of oxygen through the membrane. Modeling was performed using Finite Element Analysis. The software used to implement the mesh and solve the equations was COMSOL Multiphysics 3.5 and its Chemical Engineering toolbox.

2.3.1 Domain definition

Three different coupled domains were considered: permeate compartment, membrane and feed compartment.

The geometry of the three domains is axis-symmetric and flow is introduced in axial position; as a consequence, the solution for the velocity has axial symmetry and can be solved in a two-coordinate system using cylindrical coordinates. This fact reduces the computing effort to solve the problem without loss of precision.

2.3.2 Governing equations

The gas flow in the permeate and feed compartments was modeled using the implementation of the Navier-Stokes and continuity equations in cylindrical coordinates (Table 2). As there are not significant pressure gradients, the flow could be modeled considering a constant gas density in each compartment. For all the studied cases, the value of the Reynolds number in the inlet tubes was less than 35, therefore, laminar flow conditions could be assumed for the flow calculation in the compartments.

For the permeate compartment, as the oxygen concentration was low, conventional convection and diffusion were used to model the oxygen transport (Table 2). Besides, the permeate properties of the gas mixture were assumed as those of argon at 1000 °C (ρ = 0.3824 kg/m^3, μ = 6.544×10^{-5} Pa·s) [28]. The value of the oxygen diffusion in argon at this temperature was calculated according the Chapman-Enskog's theory (2.287×10^{-4} m^2/s). For the feed domain, the oxygen transport in the gaseous phase was modeled using Maxwell-Stefan Diffusion and Convection (Table 2). In this case, the oxygen diffusion is slightly coupled with the gas flow as fluid density depends on the oxygen fraction w_{O2} according to (3).

$$\rho = \frac{p}{R_g \cdot T} \left[\frac{w_{O2}}{M_{O2}} + \frac{(1 - w_{O2})}{M_{N2}} \right]^{-1} \tag{3}$$

The multicomponent Maxwell-Stefan diffusivities (Supporting Material) for the mixture of nitrogen and oxygen were estimated from the Fick's diffusivity that was calculated with Eq. (2) based on the kinetic gas theory [29]:

$$D_{O2,N2} = \frac{k_d \cdot T^{1.75} \cdot \left(M_{O2}^{-1} + M_{N2}^{-1} \right)^{1/2}}{p \cdot \left(v_{O2}^{1/3} + v_{N2}^{1/3} \right)^2} \tag{4}$$

where $k_d = 3.16 \cdot 10^{-8}$ Pa·m^2·s^{-1}, and the molar volumes are $v_{O2} = 1.66 \times 10^{-5}$ mol/m^3 and $v_{N2} = 1.79 \times 10^{-5}$ mol/m^3.

In the membrane, the transport of oxygen was modeled by a Fickian diffusion mechanism of oxygen vacancies in the structure (5). The transport depends on the concentration gradient of oxygen vacancies and a diffusion coefficient which is a material property.

$$\vec{J}_{vO} = -D_{vO} \cdot \nabla c_{v0} \tag{5}$$

2.3.3 Boundary conditions

First flow calculations performed with the whole size of the experimental set-up showed the areas where the flow was either almost stagnant (lower part of the feed) compartment or with a profile completely established (gas outlets). Therefore, the geometry length was cut out letting the area with relevant flow changes and setting appropriate boundary conditions. For example, the slip boundary condition was set at the bottom where stagnant flow conditions were observed. These geometry simplifications made possible to use more refined meshes in the remaining domain. The boundary definition of the system also involved the use of laminar inflow condition for both gases and to set the pressure of the gas outlets at the reference pressure (Tables 3 and 4).

The boundary conditions related with oxygen transport are shown in Tables 3 and 4. The coupling between the membrane domain and the permeate domain required to relate, at the interface, the molar flow of oxygen and the flow of oxygen vacancies using a boundary extrusion coupling variable according to stoichiometry (Table 5). Similarly, the mass flow of oxygen and the flow of oxygen vacancies were related at the feed-permeate interface by the coupling defined in Table 5.

2.3.4 Meshing

Figure 3 shows a detail of the meshes used for the geometry of the dimensions of the experimental rig. In order to ensure that the solution obtained was grid independent, the necessary level of the refining mesh was studied for the reference case. The mesh was gradually refined starting from a coarse mesh (250 elements). For a total number of cell elements greater than 9000, we observed that the modulus of the relative error of the oxygen balance for the entire rig was less than 0.1% (Figure S6). The meshes were refined at the

interfaces between domains and the areas with changes of flow direction that were detected in the preliminary calculations.

For the reference case, the final numbers of mesh elements was 1568 for the membrane geometry and 4440 and 3100 for the permeate and feed compartment, respectively. For the geometries analyzed in the parametric study a similar mesh refining was applied, e.g., Table S1 shows the effect of the mesh size on the solution accuracy (error in the oxygen mass balance) for some geometries.

2.3.5 Solver and convergence criterion

To solve the Navier-Stokes equations, the use of Lagrange elements with velocity variables approximated by quadratic polynomials and pressure by linear shape function was considered convenient. The stabilization technique was optimized for this type of elements using streamline diffusion (Galerkin-Least Squares) combined with cross-wind diffusion.

The discretization of the set of differential equations followed the general methodology of the Finite Elements method for stationary problems [30]. The resulting non-linear system of equations was solved iteratively using a damped Newton method because of the high non-linearity of the problem. The stationary direct solver used in the iteration was the UMFPACK (un-symmetric multi-frontal method), which is appropriate for small and medium size problems.

To facilitate the convergence of the problem, the flow was previously solved in the gaseous domains without considering permeation. Next, diffusion in the membrane was obtained. The solution obtained was the initial solution for the coupled problem in which diffusion in the membrane and the compartments is solved with gas flow at the same time. Parametric continuation was used in the parametric studies, i.e., a parameter was moved and the previous solution was the starting solution.

The convergence criterion was based on a weighted Euclidean norm for the estimated relative error; for each run, the nonlinear-solver iterations were stopped when the relative error calculated using Eq. (6) was less than a relative tolerance of 10^{-6}.

$$err = \sqrt{\frac{1}{N}\sum_{i=1}^{N}\left(\frac{|E_i|}{|U_i|}\right)^2}$$

(6)

where E is the estimated error in the current approximation of the true solution vector U calculated for the number of degrees of freedom N.

2.4. Fitting of the vacancy diffusion

The developed model is able to calculate the local oxygen flux on the domains and their boundaries when the diffusion coefficient of oxygen vacancies in the ceramic membrane (D_{VO}) is known. Then, the oxygen flow through the membrane can be obtained by boundary integration. The diffusion coefficient corresponding to an experimental value of oxygen flow was obtained using the quadratic interpolation technique shown in Figure 4. In this calculation procedure, the value $D_{VO}*$ has been interpolated for the average experimental flux and the two values that yield to values of flux near to the experimental flux are saved for the following iteration.

2.5. Parametric study

The reference case considered in the study (Table 1) corresponds to the experimental rig employed in the permeation experiment. We assumed that the parameter D_{VO} does not depend significantly on the oxygen vacancy concentration in the considered p_{O2} range and, therefore, it was maintained constant in the parametric study.

(1) In the study of the geometry of the permeate compartment, the distance between the inlet and the membrane was varied from 1 to 9 mm while the radius of the inlet tube was studied in the range from 0.5 to 4 mm (the radius of the permeate compartment was 5.75 mm). The geometry of the feed compartment corresponds to the reference case.

(2) In study of the geometry of air compartment, the same ranges were applied for the variation of the inlet distance from the membrane and the radius of the air inlet tube. The geometry of the permeate compartment corresponds to the reference case.

(3) The study of the gas inlet flow rate was performed varying it in the range from 12.5% to 400% of the reference flow for the reference geometry and selected rig geometries. The flow rate was varied independently in each compartment.

3. RESULTS AND DISCUSSION

In this section, three magnitudes (flow streamlines, oxygen concentration and oxygen flow rate) has been analyzed in the different set-up volumes in order to

determine the influence of the different geometric and operational factors on fluid dynamics and therefore on the final permeation. Moreover, two figures of merit, i.e., average oxygen flux through the ceramic membrane and average oxygen concentration on the corresponding membrane surface, have been selected to show the goodness and incremental improvements of the fluid dynamics through geometry and inlet flow rate variations.

3.1 Calculation of diffusion coefficient in the membrane and oxygen profiles for the reference case

For the reference case, the experimental average flux on the membrane was of 0.078 μmol·cm^{-2}·s^{-1}. For this value, the iterative procedure explained in section 2.4 yielded a value of the oxygen vacancy diffusion in the membrane of D_{VO} = 6.05×10^{-9} m^2·s^{-1}. This value is slightly higher than one value obtained experimentally [27, 31] (~7.4×10^{-10} m^2·s^{-1}). This difference may stem from the different experimental techniques employed and the fact that polarization concentration issues are corrected in our calculation. Figure 5 to 7 show the computed oxygen flow and oxygen concentration distribution in the three different considered volumes obtained with the converged value of D_{vo}. The oxygen concentration distribution and streamlines are available in Supporting Material (Figure S1) for the three considered volumes. Figure 5 shows the flow streamlines and the oxygen molar fraction in the air feed compartment. There can be seen that the concentration gradient is higher in the area between the inlet and the membrane and in the rest of the compartment the oxygen concentration is almost constant. Nevertheless, the absolute variation of the oxygen concentration between the proximity of the membrane and the feed gas is very small due to the large difference between the fed oxygen flow rate (in air stream) and the permeation flux across the membrane. Consequently, polarization effects in the air feed compartment are negligible from the point of view of the permeation driving force for the conditions considered here.

Figure 6 shows the distribution of oxygen vacancies in the membrane. Note the high vacancy concentration at the permeate side of the membrane compared to the feed side, which is consistent with the oxygen-vacancies equilibrium. Due to the necessary seal the external annulus of the membrane disc is not in contact with the gaseous phases (See also Figure S1). However some of the oxygen transport is by-passed by this area. This fact must be taken into account to calculate the effective flux through the membrane.

The streamlines in the permeate compartment (Figure 7) show that an important fraction of the sweep-gas flow does not approach to the membrane and "leak" directly toward the permeate outlet. As a consequence, an important concentration polarization effect is produced and the oxygen concentration measured in the permeate outlet does not corresponds to the true oxygen concentration on the membrane surface. Therefore, the driving force estimated experimentally typically by GC or MS analysis of the outlet gas stream is significantly higher than the real one. Moreover, the relative changes in concentration in the permeate compartment are much more important than in the air feed chamber (See also Figure S1). For the geometry and operating conditions corresponding to the reference case, there are not significant important oxygen concentration gradients along the membrane surface, i.e., radial gradients, due to the important polarization in the vertical axis direction.

As previously mentioned, the calculated value of D_{VO} is assumed to be independent from the concentration in the studied oxygen partial pressure range and then it is maintained constant in the following parametric study.

3.2 Effect of geometry on the oxygen transport in the air feed compartment

It was studied (Figure S2) the variation of **(1)** the distance between the air inlet tube and the membrane on the average oxygen flux (permeation flux) and **(2)** the average oxygen partial pressure on the membrane surface. It can be seen that there are only minor changes on both figures of merit. Indeed, for an increment on the inlet distance of 3.5 mm, a variation of 0.06% and -0.03% is achieved for oxygen concentration and flux, respectively. A similar result is obtained when the inlet gas radius was varied (Figure S3). The small relative variations of the logarithm of oxygen partial pressure in the feed chamber led to very small variations on the concentration of oxygen vacancies in the feed side. As a consequence, there is a small variation of the driving force for oxygen transport and it can be concluded that the variations on the geometry in the air compartment influence the fluid dynamics although this changes have a minor impact on the oxygen concentration on the surface membrane, i.e., on the oxygen permeation flux through the membrane. Therefore, oxygen flux may be principally determined by the conditions on the permeate compartment.

3.3 Effect of geometry on the oxygen transport in the permeate compartment

In contrast to the observations in the air feed compartment, the polarization effects in the permeate compartment had a remarkable influence on the oxygen concentration on the membrane surface and as a consequence on the oxygen transport through the ceramic membrane. In Figure 8, it can be seen the effect of applying different distances between sweep-gas inlet tube (Z) and membrane surface on the oxygen pressure profile for a constant inlet radius corresponding to the reference case (R = 1.5 mm).

A smaller distance between sweep-gas inlet and membrane surface led to the noteworthy decrease of oxygen concentration on the different radial positions of the membrane surface although a much less homogenous distribution of oxygen on the membrane surface is observed. Figure S4 shows the 2D oxygen concentration distribution and streamlines in the permeate volume for three different distances (Z = 5, 3, 1 mm). There can be confirmed the reduction of the polarization and the increase in the permeation rate although a much important radial gradient of oxygen concentration on the membrane surface is observed for small Z distances due to the strong reduction of the oxygen concentration on the central part of the membrane. Specifically, the higher oxygen concentration reduction for Z = 1 corresponds to a radial distance (Figure 8) similar to the inlet tube diameter and for higher radial distances the concentration increases steeply. Therefore, it was decided to study the coupled effect of the variation of these two geometric parameters. Indeed, Figure 9 shows the effect of modification of the sweep-gas inlet radius (from 0.5 to 4 mm) for three different inlet positions (Z = 1, 3 and 7 mm) on the oxygen concentration along the membrane surface (radial coordinates). For all three inlet positions, a smaller sweep-gas inlet radius implies a less homogenous distribution of oxygen on the membrane surface. Furthermore, this effect is higher when the inlet distance to the membrane is smaller. Close to the center of the membrane there exists an efficient sweeping cone/plume whose radius is closely related to the inlet diameter, especially when the gas inlet tube is very close to the membrane surface (Figure 11a- Z= 1 mm).

A better understanding of this behavior can be obtained by analyzing the average oxygen flux and oxygen concentration through the membrane for the different cases. The average oxygen concentration for the whole membrane area was calculated from the concentration profiles on the corresponding membrane surface. In Figure 10a, the lowest oxygen concentration values, i.e., lowest polarization, are obtained for the shortest inlet distance and an inlet radius above 2.5 mm. Moreover, the effect of the reduction of the inlet radius is more important for large inlet distances. This is ascribed to the fact that a small radius involves a higher sweep-gas velocity of the gas reaching the membrane surface, i.e., a longer sweep *plume*, and therefore there is more sweeping efficiency of the membrane surface, at least in the central part of the

membrane. On the contrary, for short Z distances, a small inlet radius involves a lower sweeping efficiency on the outer part of the membrane surface. Figure 10b shows the influence of a large number of Z distances on the average surface oxygen concentration. The most important observation is that the inlet distance is more important that the inlet radius. Specifically, the variation of the inlet radius has a minor effect when the radius is higher than 1 mm. Nevertheless, for the smallest inlet diameter (0.5 mm), a significant reduction of the oxygen concentration is observed when Z ≥ 4.5mm while a detrimental effect at short Z distances is stated, as previously mentioned.

Figure 11 presents the influence of these two geometric parameters (Z and R) on the average oxygen flux. This figure confirms the conclusions extracted from Figure 10, since the oxygen distribution in the permeate compartment, i.e., driving-force for oxygen transfer is directly but non-linearly related to the average flux. Concretely, the impact of the geometric parameters on the flux is slightly smaller than that observed in the oxygen concentration due to the non-linear expression of the chemical potential gradient across the membrane. The highest oxygen flux is reached for the shortest inlet distance (R = 1 mm) in combination with the largest inlet diameter, although the influence of the radius on the flux is negligible when R ≥ 1 mm and Z = 1 mm (See for instance Figure 11b).

3.4   Parametric study of the effect of gas inlet flow rate

The increase of sweep-gas inlet flow rate allows decreasing strongly the average oxygen pressure (Figure 12a), i.e., diminishing the polarization on the permeate membrane side and therefore a notable increase in the oxygen flux through the membrane is achieved (Figure 12b). The strong improvement in the sweeping efficiency can be observed in Figure S5, where the streamlines and oxygen concentration are shown in the permeate compartment volume for three different sweep gas flow rates, i.e., 50, 100 and 200 cm^3(STP)/min. However, here it should be noted that the increase in the sweep gas flow rate can cause problems of temperature gradients in the gas compartments and solid state membrane if the gas is not properly pre-heated before introduction in the permeation compartments. This aspect can be particularly critical for very high operating temperature (e.g. 1000ºC) and high gas flow rates, typically higher than 100 cm^3(STP)/min. On the contrary, the air inlet flow does not have any significant effect on both oxygen surface concentration and permeation flux because, as previously stated, the relative variations of oxygen composition in

the air compartment are smaller for the considered membrane thickness and perovskite composition.

Finally, it was studied the combined influence of sweep-gas inlet distance and inlet flow rate on the oxygen concentration and oxygen flux (Figure 13). Figure 13b includes the experimental oxygen flux obtained for the reference case geometry when the sweep-gas flow rate is varied. These results follow the computed trend within the experimental error (Note that the flux for Z=7 is the one used in the determination of D_{VO}). The inlet gas flow rate seems to be the most important parameter studied and the proper choice of the flow rate is more critical than the inlet distance choice. Nevertheless, the inlet distance is significant even at the highest flow rate (200 cm^3(STP)/min) as seen in Figure 12b. The effect of the sweep-gas flow rate variation was similar for the different inlet distances to membrane (Z). However, the effect of the variation of the inlet distance is smaller for high sweep-gas flow rates as a consequence of the general improvement in the sweeping efficiency.

4. CONCLUSIONS

The oxygen transport in a lab-scale experimental rig for characterization of ceramic membranes has been modeled taking into account gas hydrodynamics and oxygen diffusion in the gas phase and vacancy diffusion of oxygen in a perovskite membrane. The rig geometry and feed flow rate had a significant effect on the oxygen transport through the membrane. The model was useful to obtain the coefficient diffusion of oxygen vacancies which is a material property. The parametric study showed that the geometry and flow in the air compartment did not have significant influence on the oxygen transport, at least for moderate oxygen flux through the membrane. However, there were very important polarization effects in the sweep-gas compartment. For example, to approach the sweep-gas inlet to the membrane caused an important reduction in the oxygen concentration near the membrane surface, and consequently an increment of the oxygen flux. The best sweeping efficiency, i.e., the highest oxygen flux, was obtained for the following conditions (in increasing order of importance): (1) large gas inlet radius; (2) short gas inlet distance (Z = 1 mm); and (3) high gas flow rate, e.g. 200 cm^3(STP)/min. Future CFD modeling on this kind on membranes should tackle (i) the influence of other geometric factors and other membrane configurations as well as contrasting the CFD calculations with experimental results; (ii) the effect of the reduction of the thickness and/or increase of the membrane permeability; (iii) surface exchange limitations and presence of porous catalytic layers; among others.

LIST OF SYMBOLS

c_{O2} concentration of oxygen in gas, mol/m^3

c_{VO} concentration of oxygen vacancies in the membrane, mol/m^3

$D_{i,j}$ diffusion coefficient of component i in component j, m^2·s^{-1}

D_{VO} diffusion coefficient of oxygen vacancies in the membrane, m^2·s^{-1}

g_z z-component of gravity acceleration, m·s^{-2}

J_{O2} molar flux of oxygen, mol·m^{-2}·s^{-1}

J'_{O2} mass flux of oxygen, g·m^{-2}·s^{-1}

J_{exp} average experimental flux, mol·m^{-2}·s^{-1}

J_{VO} average flux obtained for diffusion coefficient D_{VO} , mol·m^{-2}·s^{-1}

k_d coefficient for calculation of diffusivity, Pa·m^2·s^{-1}

M_i molecular weight of component i, g·mol^{-1}

N_i molar flux of component i

N'_i mass flux of component i

n_{S12} vector normal to surface from sweep-gas domain to membrane

n_{S21} vector normal to surface from membrane to sweep-gas domain

n_{S23} vector normal to surface from membrane to air feed domain

n_{S32} vector normal to surface from air feed domain to membrane

p total pressure, atm

p_{O2} partial pressure of oxygen, atm

Q gas flow rate, cm^3(STP)/min

r feed inlet radius (inner tube radius), mm

R sweep-gas inlet radius (inner tube radius), mm

R_g gas perfect constant, 8.315 J·mol^{-1}·K^{-1}

T temperature, K

U velocity vector, m·s^{-1}

u_r r-component of velocity, m·s^{-1}

u_z z-component of velocity, m·s^{-1}

v_i molar weight of nitrogen, mol·m^{-3}

w_i mass fraction of component i

x_i mass fraction of component i

z distance of air feed inlet to membrane, mm

Z distance of sweep-gas inlet to membrane, mm

Greek letters

η gas viscosity, Pa·s

ρ gas density, kg/m^3

ACKNOWLEDGEMENTS

REFERENCES

[1] J. Sunarso, S. Baumann, J. M. Serra, W.A. Meulenberg, S. Liu, Y.S. Lin, J. C. Diniz da Costa, *J. Memb. Sci.* 320 (2008) 13-41

[2] S. Engels, F. Begge, M. Modigell, H. Stadler, J. Membrane Sci. 359 (2010) 93-101

[3] I. Pfaff, A. Kather, Comparative thermodynamic analysis and integration issues of CCS steam power plants based on oxy-combustion with cryogenic or membrane based air separation, Energy Procedia 1 (2009) 495–502.

[4] H. H. Wang, S. Werth, T. Schiestel, J. Caro, Angew. Chem. 44 (42) (2005)6906

[5] H. J. M. Bouwmeester, *Catal. Today* 82 (2003) 141-150

[6] L. Olivier, S. Haag, C. Mirodatos, A.C. van Veen, *Catal. Today* 142 (2009) 34

[7] F. T. Akin and Y. S. Lin, *Catal. Letters* 78 (2002) 1.

[8] M. Trunec, J. Cihlar, S. Diethelm, J. Van Herle, *J. Am. Ceram. Soc.* 89 (3) (2006) 955

[9] J. Pérez-Ramírez, B. Vigeland, Angew. *Chem. Int.* Ed. 44 (2005) 1112

[10] Y. Y. Liu, X. Y. Tan, K. Li, Catal. *Rev. Sci. Eng.* 48 (2) (2006): 145

[11] J. M. Serra, V. B Vert, O. Büchler, W. A. Meulenberg, H.-P. Buchkremer, *Chem. Mat.* 20 (2008) 3867

[12] R. Ghidossi, D. Veyret; P. Moulin, Computational fluid dynamics applied to membranes: State of the art and opportunities, *Chem. Eng. Proces.* 45 (2006) 437-454

[13] M. K. Koukou, N. Papayannakos, N. C. Markatos, M. Bracht, H. M. Van Veen, A. Roskam, *J. Membrene Sci.* 155 (1999) 241-259

[14] H. Takaba, S. Nakao, *J. Membrane Sci.* 249 (2005) 83-88

[15] M. Coroneo, G. Montante, M. G. Baschetti, A. Paglianti, Chem. Eng. Sci. 64 (2009) 1085-1094

[16] C. Siegel, Review of computational heat and mass transfer modeling in polymer-electrolyte-membrane (PEM) fuel cells, *Energy* 33 (2008) 1331-1352

[17] R. Sousa Jr., D. Marques dos Anjos, G. Tremiliosi-Filho, E. Rafael-González, C. Coutanceau, E. Silbert, J.M. Léger, K. Boniface-Kokoh, *J. Power Sources.* 180 (2008) 283-293

[18] T. X. Ho, P. Kosinski, A.C. Hoffmann, A. Vik, Numerical modeling of solid oxide fuel cells, *Chem. Eng. Sci.* 63 (2008) 5356-5365

[19] N. Akhtar, S.P. Decent, D. Loghin, K. Kendall, A three-dimensional model of a single-chamber solid oxide fuel cell, *Int. J. Hydrogen Energy* 34 (2009) 8645-8663

[20] K.-D. Tigges, F. Klauke, C. Bergins, K. Busekrus, J. Niesbach, M. Ehmann, C. Kuhr, F. Hoffmeister, B. Vollmer, T. Buddenberg, Song Wu, Allan Kukoski, Conversion of existing coal-fired power plants to oxyfuel combustion: Case study with experimental results and CFD-simulations, *Energy Procedia* (2009) 549–556

[21] S. Engels, F. Beggel, M. Modigell, H. Stadler, Simulation of a membrane unit for oxyfuel power plants under consideration of realistic BSCF membrane properties, *Journal of Membrane Science.* 359 (2010) 93-101.

[22] J.C. Ramirez, M. Stan, P.Cristea, Simulations of heat and oxygen diffusion in UO_2 nuclear fuel rods, *J. Nuclear Mater.* 339 (2006) 174-184

[23] J.M. Gozálvez-Zafrilla, J.M. Serra, A. Santafé-Moros; *Modeling of High-Temperature Ceramic Membranes for Oxygen Separation* in Proceedings of the COMSOL European Conference (2009) Hannover

[24] J.M. Serra, J. M. Gozálvez-Zafrilla, A. Santafé-Moros, S. Escolástico, *Dynamic Modeling of Oxygen Permeation through Mixed Ionic-Electronic Conducting Membranes* in Proceedings of the NAMS/ICIM 2010, 17-22 July 2010, Washington (USA)

[25] S. Engels, M. Modigell, *CFD-based inverse analysis of mass transfer through oxygen transfer membranes* in Proceedings of the NAMS/ICIM 2010, 17-22 July 2010, Washington (USA)

[26] B. Rüger, A. Weber, E. Ivers-Tiffee, ECS Transactions 7 (2007) 2065-2074

[27] B. A. van Hassel, T. Kawada, N. Sakai, H. Yokokawa, M. Dokiya, Oxygen permeation modelling of perovskites, Solid State Ionics, 66 (1993) 295-305

[28] E.W. Lemmon R.T. Jacobsen, Viscosity and Thermal Conductivity Equations for Nitrogen, Oxygen, Argon, and Air, *International Journal of Thermophysics*, Vol. 25, 1, (2004) 21-69

[29] J. A. Wesselingh, R. Krishna, *Mass Transfer in Multicomponent Mixtures*, Delft University Press (2000)

[30] W. B. Zimmerman, Process Modelling and Simulation with Finite Element Methods, World Scientific, Singapore (2004

[31] T. Ishigaki, S. Yamauchi, K. Kishio, J. Mizusaki, K. Fueki, J. Solid State Chem. 73 (1988) 179

Figure Captions:

Figure 1. (a) Schematics of the experimental set-up and (b) detail of the membrane area.

Figure 2. Calculated equilibrium between oxygen partial pressure in the gas and oxygen vacancy mol fraction in the solid ($La_{0.9}Sr_{0.1}FeO_{3-\delta}$).

Figure 3. Detail of the meshes used in the three different domains.

Figure 4: Iteration procedure of the diffusion coefficient of oxygen flux vacancies.

Figure 5: Flow streamlines and oxygen molar fraction profiles in feed compartment for the reference case

Figure 6: Mol fraction profiles of oxygen vacancies in the membrane for the reference case

Figure 7: Flow streamlines and oxygen molar fraction profiles in permeate compartment for the reference case

Figure 8: Oxygen partial pressure on the membrane surface of the permeate side as a function of the radial distance for different inlet distances to membrane (R = 1.5 mm)

Figure 9: Oxygen partial pressure on the membrane surface of the permeate side as a function of the radial distance for different inlet radius and inlet distances to membrane (a) Z= 1 mm, (b) Z = 3 mm, (c) Z = 7 mm

Figure 10: Average oxygen partial pressure on the membrane surface of the permeate side as a function of (a) the inlet radius for different inlet distances to membrane and (b) the inlet distance for different inlet radii.

Figure 11: Average oxygen flux (permeation flux) as a function of (a) the inlet radius for different height positions and (b) the inlet distance to membrane for different inlet radii (permeate compartment).

Figure 12: Average oxygen partial pressure (a) and oxygen flux (b) on the membrane surface as a function of the inlet flows for the geometry of the reference case (Q_{ref} = 50 cm^3(STP)/min).

Figure 13: Average oxygen partial pressure (a) and oxygen flux (b) on the membrane surface as a function of the sweep-gas inlet flows for the three inlet distances to membrane (Z= 1, 3 and 7 mm; Q_{ref} = 50 cm^3(STP)/min and R = 1.5 mm). The experimental oxygen flux corresponding to the base case is included in the (b) chart when the sweep gas flow rate was varied.
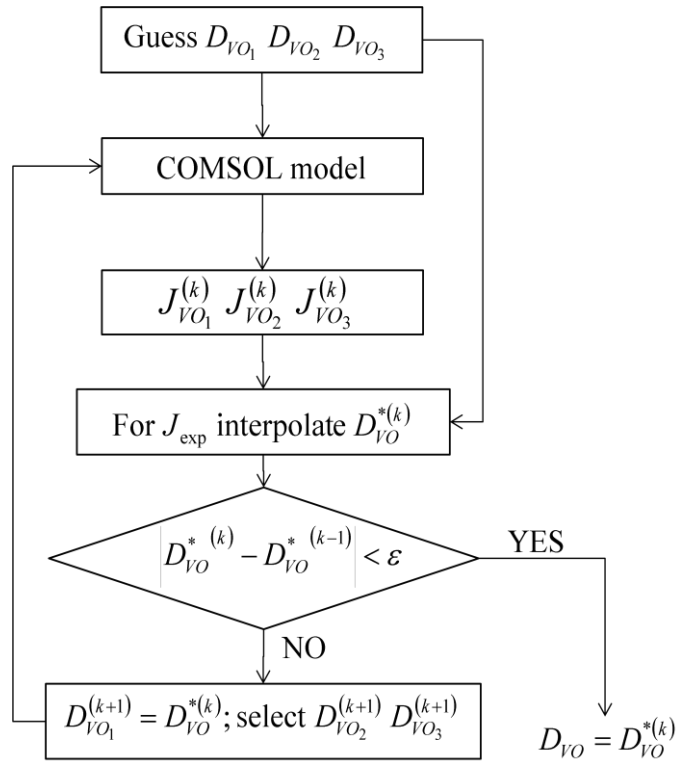
Figure 1

Figure 2

Figure 3

sweep-gas   permeate   depleted air

(1) permeate
    compartment

(2) membrane

(3) feed
    compartment

air feed
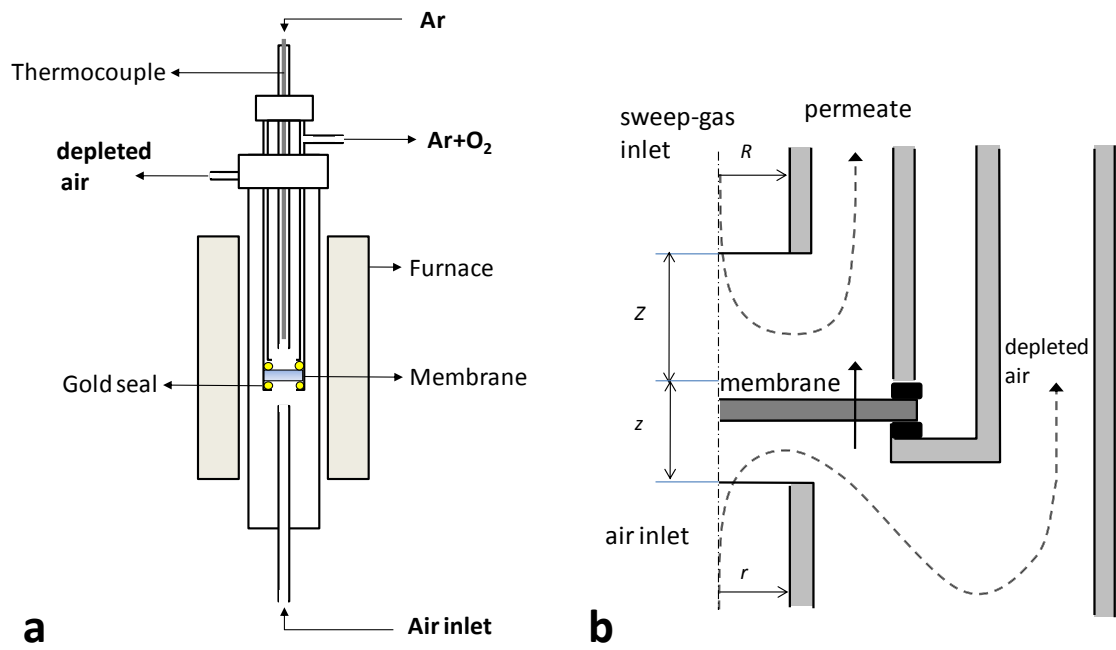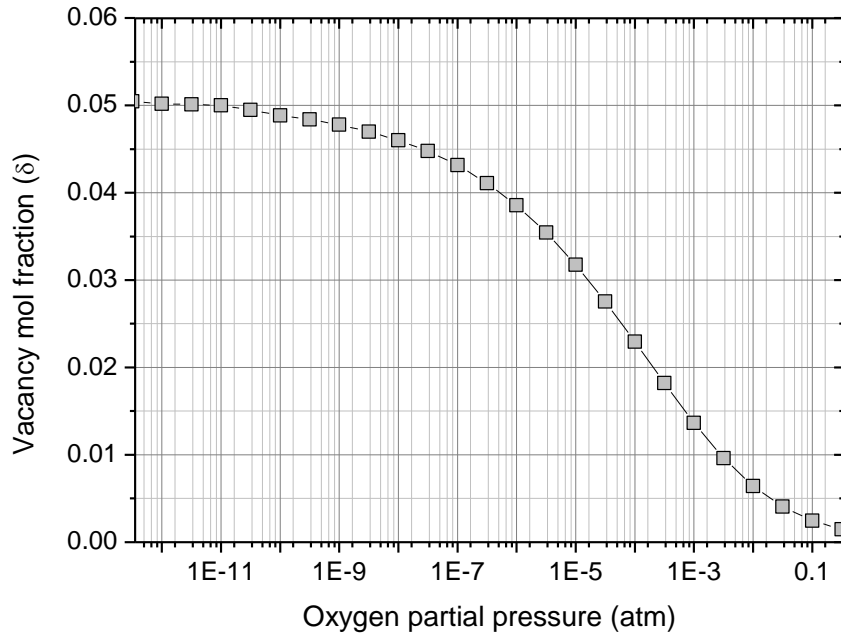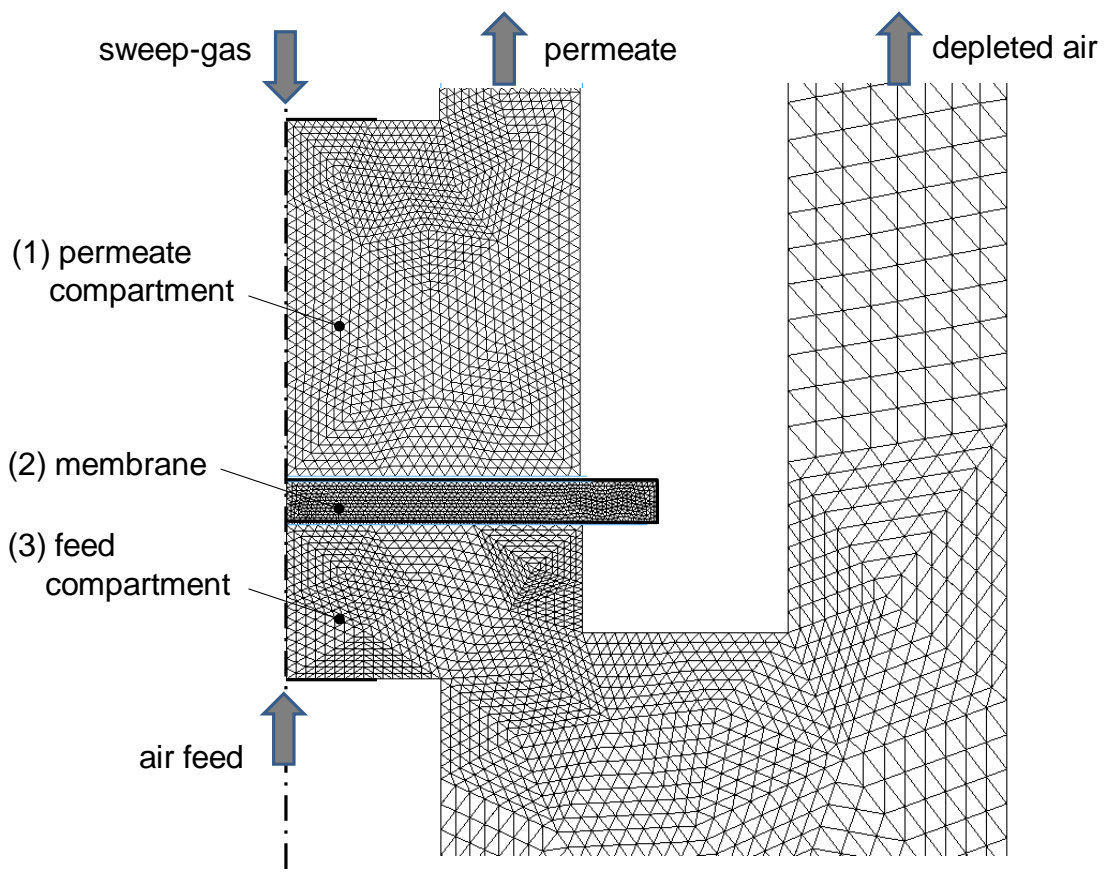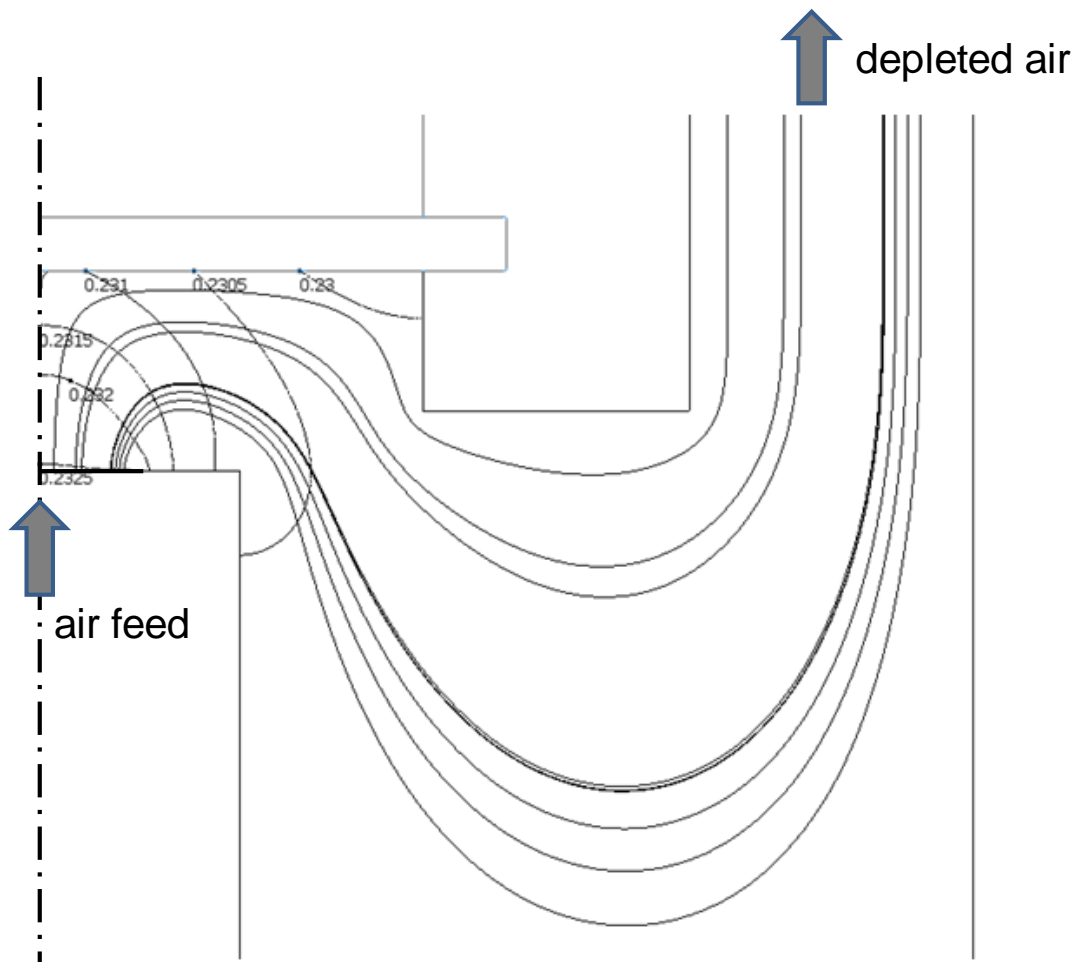
Figure 4

Figure 5

Figure 6
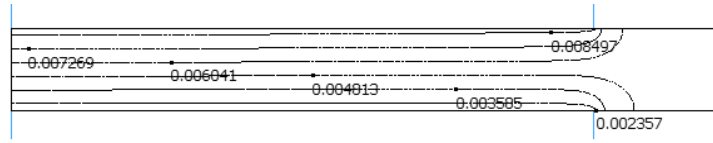
Figure 7
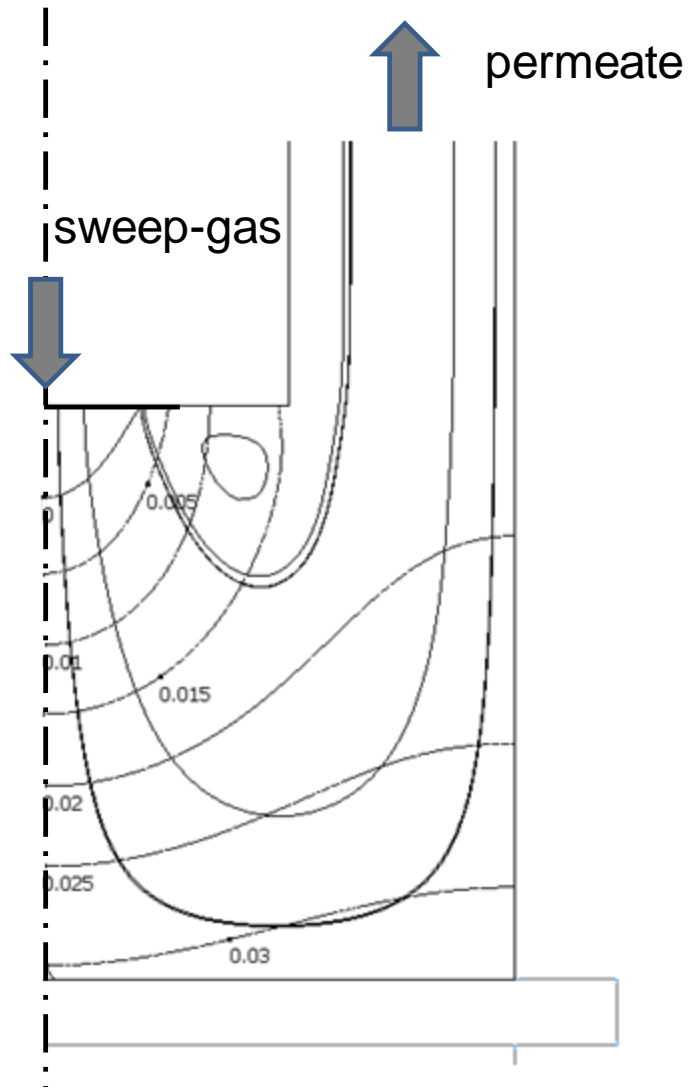
Figure 8
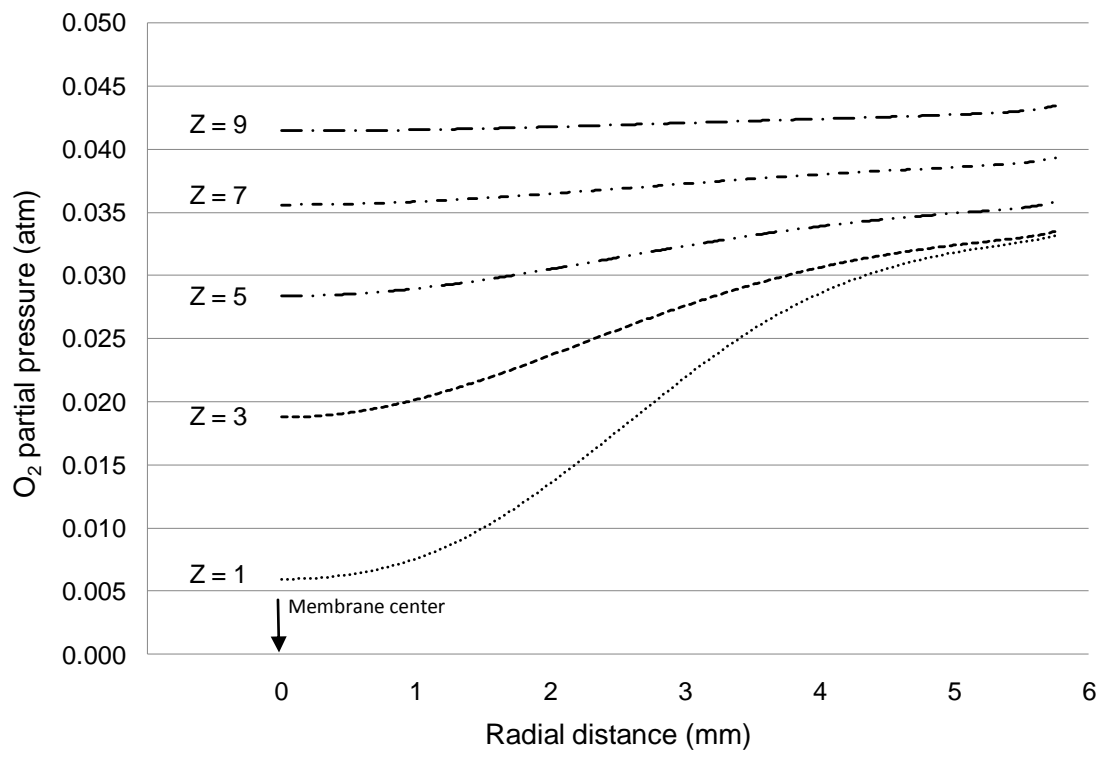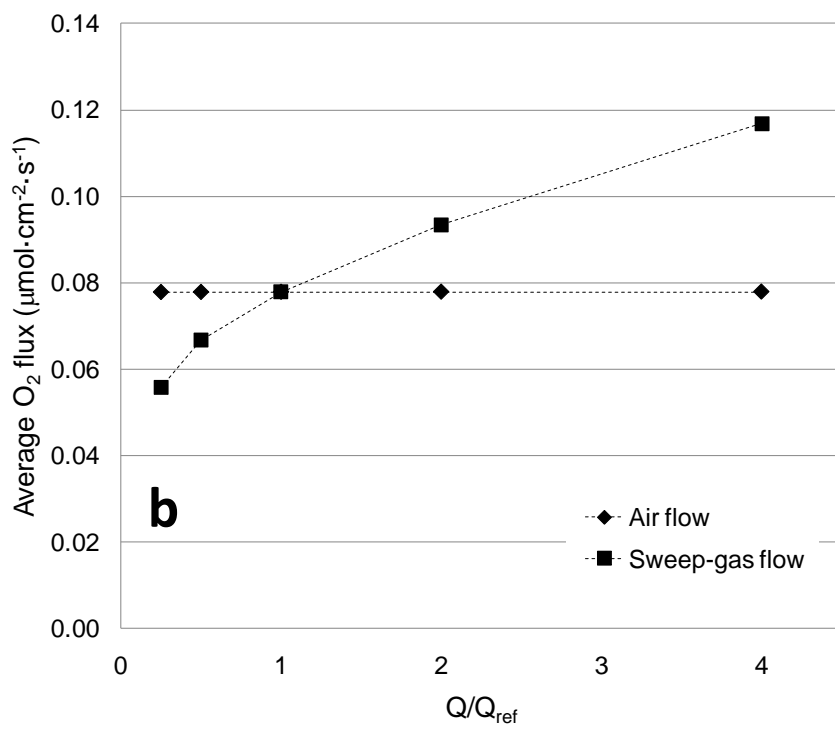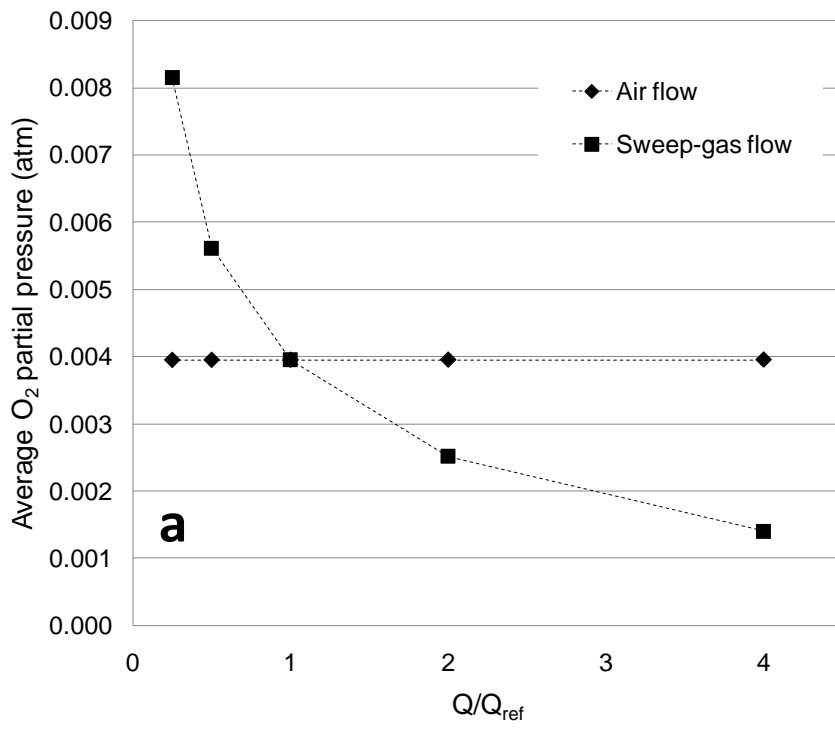
Figure 9
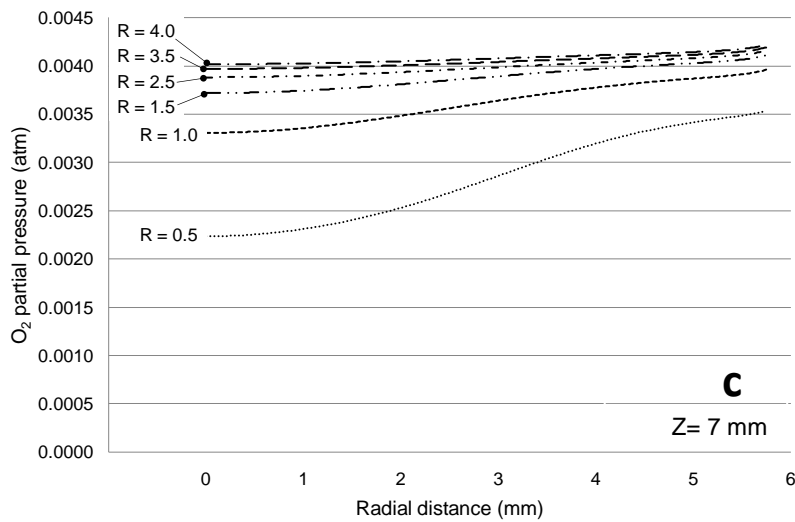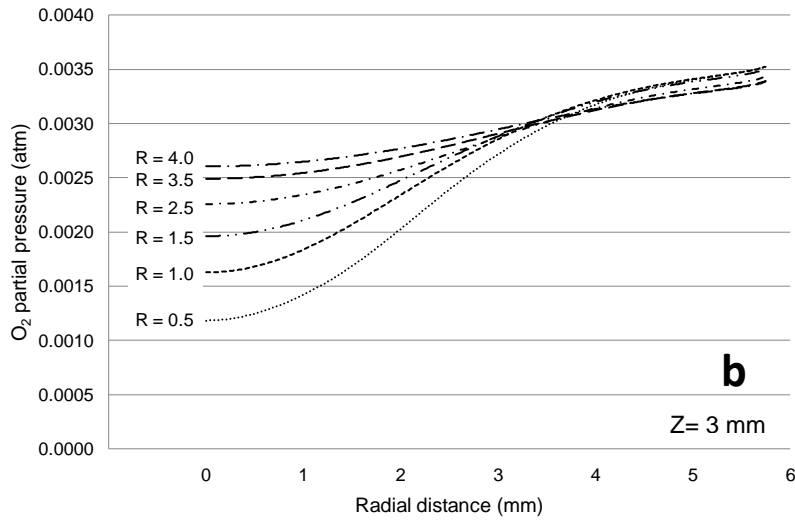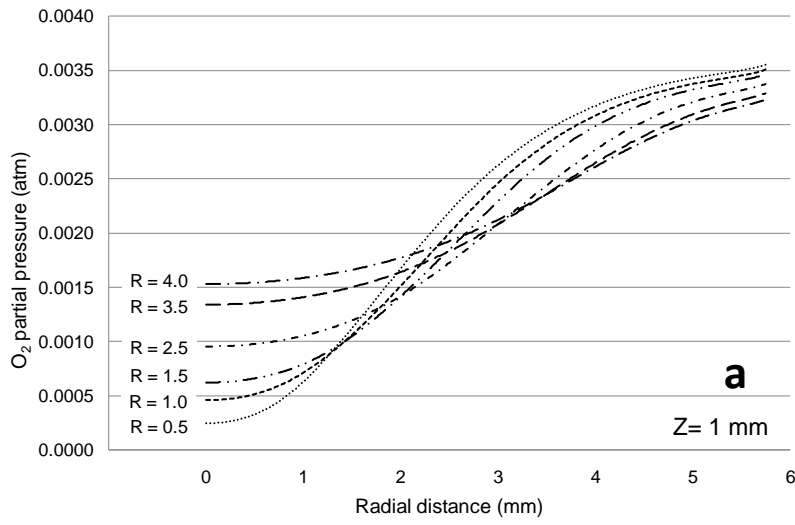
Figure 10
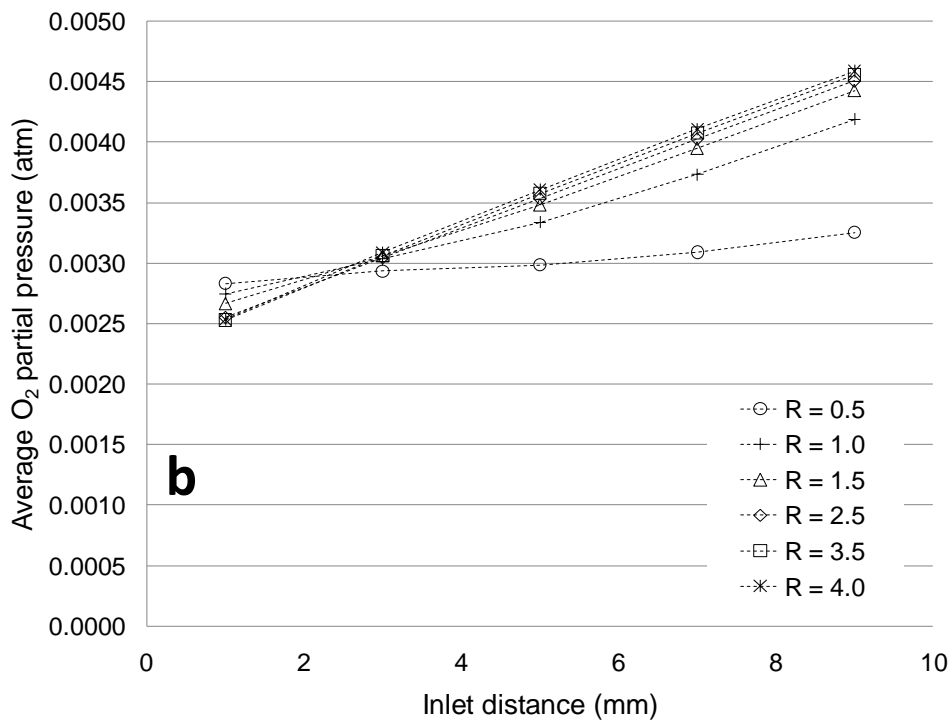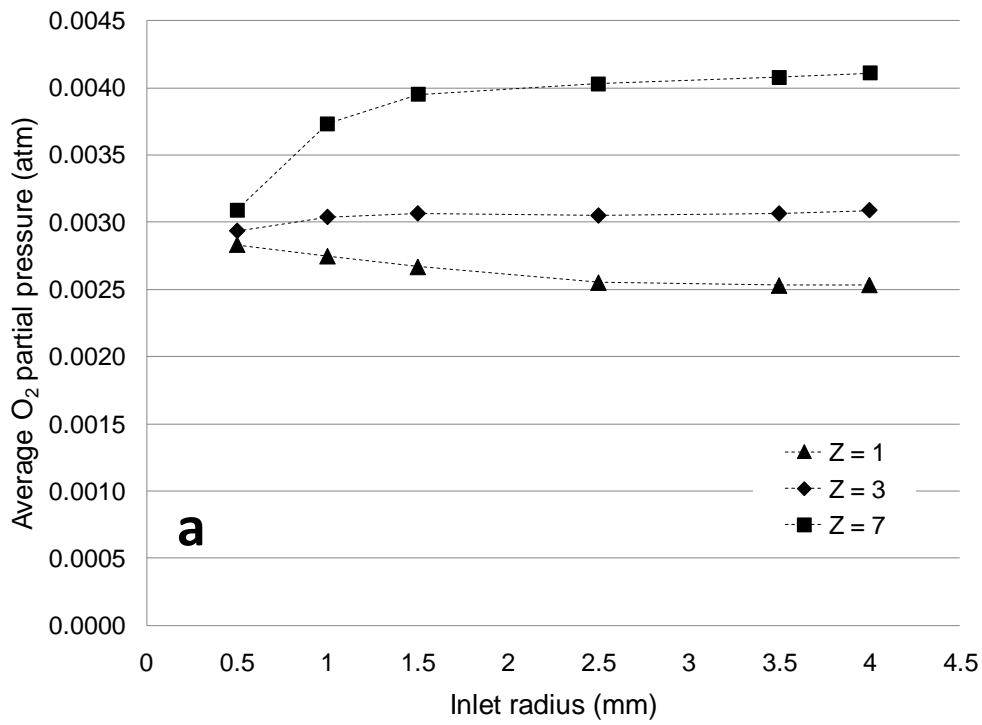
Figure 11
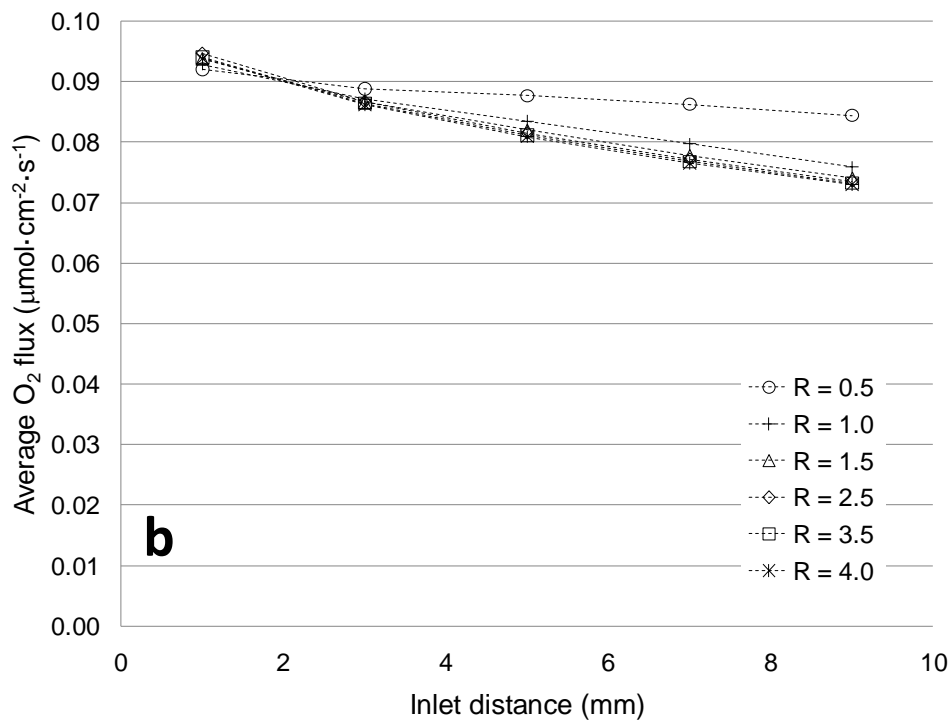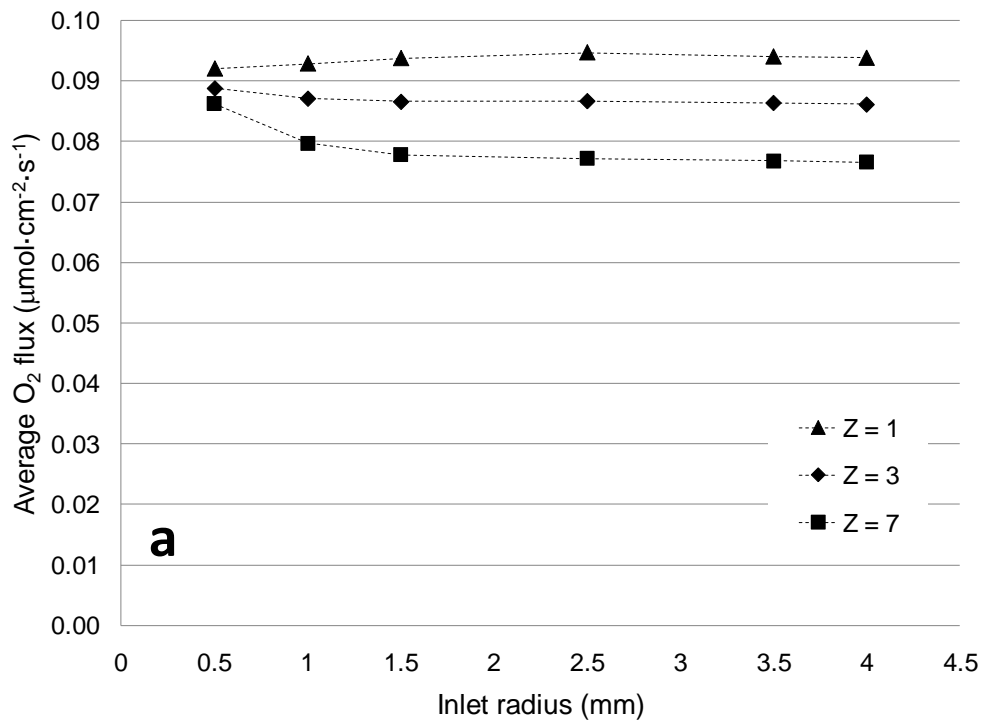
Figure 12

Figure 13
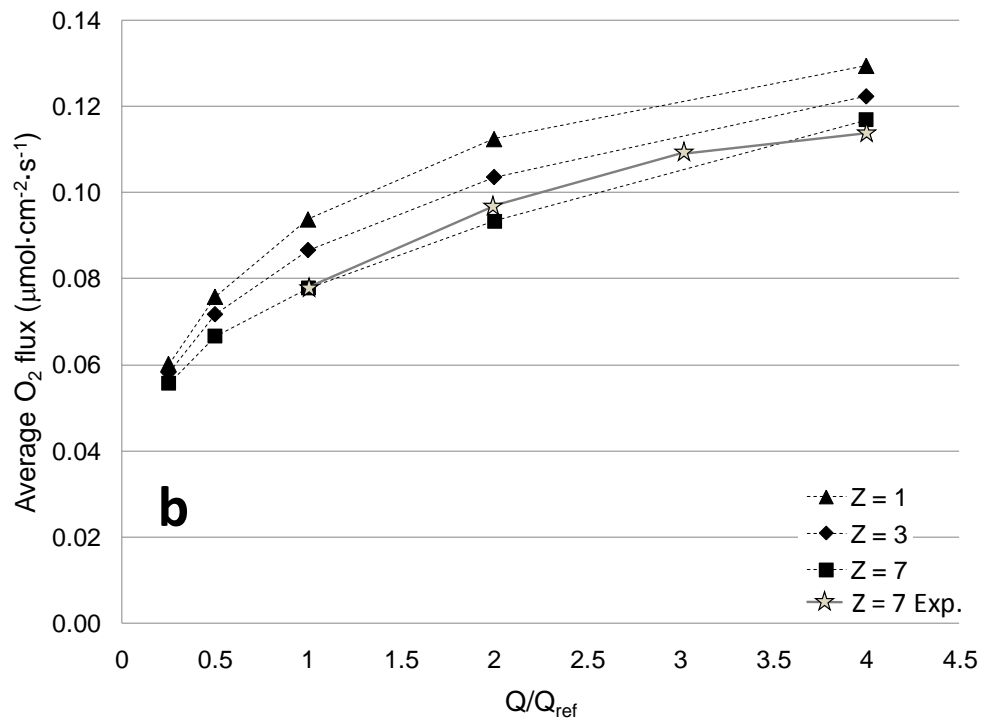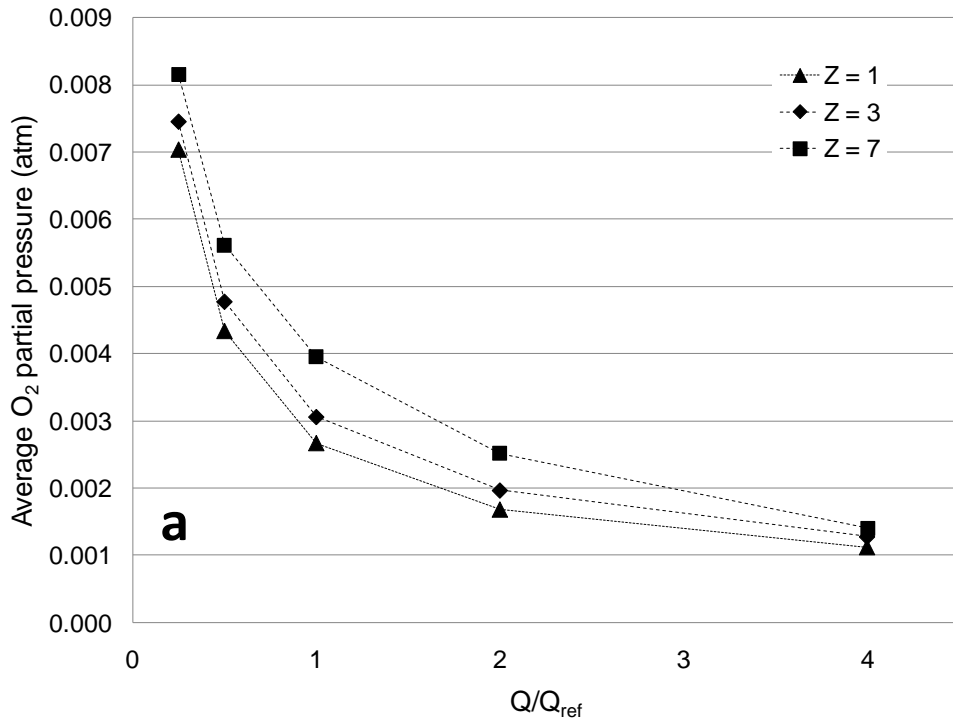
Table 1. Geometry of the experimental rig and experimental conditions (Reference case).

Variable	Units	Value
Sweep-gas inlet radius (inner tube radius), R	mm	1.5
Wall thickness of sweep-gas inlet	mm	1.5
Feed inlet radius (inner tube radius), r	mm	1.5
Wall thickness of feed inlet	mm	1.5
Distance of sweep-gas inlet to membrane, Z	mm	7
Distance of feed inlet to membrane, z	mm	3
Sweep-gas flow (argon)	cm^3(STP)/min	50
Feed flow (air)	cm^3(STP)/min	50
Temperature	°C	1000
Pressure	atm	0.02

Table 2. Governing equations of the model

a) Flow modeling in both phases

Equation for conservation of mass (continuity):

$$\frac{\partial u_r}{\partial r} + \frac{u_r}{r} + \frac{\partial u_z}{\partial z} = 0$$

Equation of Momentum (Navier-Stokes):

For r-coordinate:

$$\rho\left(u_r \frac{\partial u_r}{\partial r} + u_z \frac{\partial u_r}{\partial z}\right) = -\frac{\partial p}{\partial r} + \left[\frac{1}{r}\frac{\partial}{\partial r}\left(r\frac{\partial u_r}{\partial r}\right) + \frac{u_r}{r^2} + \frac{\partial^2 u_r}{\partial z^2}\right]$$

For z-coordinate:

$$\rho\left(u_r \frac{\partial u_z}{\partial r} + u_z \frac{\partial u_z}{\partial z}\right) = -\frac{\partial p}{\partial z} + \rho\, g_z + \left[\frac{1}{r}\frac{\partial}{\partial r}\left(r\frac{\partial u_z}{\partial r}\right) + \frac{\partial^2 u_z}{\partial z^2}\right]$$

b) Convection and Fick's diffusion of oxygen (1) in sweep gas (3):

$$\frac{1}{r}\frac{\partial}{\partial r}(r u_r c_{O2}) + \frac{\partial}{\partial z}(u_z c_{O2}) = D_{O2,Ar}\left[\frac{1}{r}\frac{\partial}{\partial r}\left(r\frac{\partial c_{O2}}{\partial r}\right) + \frac{\partial^2 c_{O2}}{\partial z^2}\right]$$

c) Diffusion of oxygen vacancies in the membrane:

$$0 = D_{Vo}\left[\frac{1}{r}\frac{\partial}{\partial r}\left(r\frac{\partial c_{Vo}}{\partial r}\right) + \frac{\partial^2 c_{Vo}}{\partial z^2}\right]$$

d) Convection and Maxwell-Stefan's diffusion of oxygen (1) in nitrogen (2) at constant temperature:

$$\nabla \cdot \left\{\rho w_{O2} \mathbf{U} - \rho w_{O2}\left(\tilde{D}_{O2,O2} - \tilde{D}_{O2,N2}\right)\left(\nabla x_{O2} + (x_{O2} - w_{O2})\frac{\nabla p}{p}\right)\right\} = 0$$

where:

$$x_{O2} = w_{O2}\frac{M_{O2} x_{O2} + M_{N2} x_{N2}}{M_{O2}}$$

$$\nabla x_{O2} = \frac{M_{O2} M_{N2}}{\left[M_{O2} + (M_{N2} - M_{O2})w_{O2}\right]^2}\nabla w_{O2}$$

Maxwell-Stefan multicomponent diffusivities:

$$\tilde{D}_{1,1} = \frac{w_2^2}{x_1 x_2}D_{1,2} \qquad \tilde{D}_{1,2} = \tilde{D}_{2,1} = -\frac{w_1 w_2}{x_1 x_2}D_{1,2}$$

e) Relations between fractions in feed:

$$w_{N2} = 1 - w_{O2}$$

$$x_{N2} = 1 - x_{O2}$$

Table 3. Boundary conditions (Flow)[1]

Domain	Boundary	Type	Value
Sweep-gas	inlet	laminar inflow	3.56 cm^3/s
	outlet	pressure	101300 Pa
	axis	axial symmetry	
	membrane	non-slip	
	wall	non-slip	
Feed	inlet	laminar inflow	3.56 cm^3/s
	outlet	pressure	101300 Pa
	axis	axial symmetry	
	membrane	non-slip	
	wall	non-slip	
	stagnant zone	slip	

[1]The values shown are for the reference case

Table 4. Boundary conditions (Diffusion)[1]

Domain	Boundary	Type	Value
Sweep-gas (convection and diffusion)	inlet	oxygen concentration	0.2 mol/m^3
	outlet	convective flow	
	axis	axial symmetry	
	membrane interface	coupling (Eq. 6)	
	wall	insulation	
Membrane (diffusion of oxygen vacancies)	sweep-gas interface	coupling (Eq. 6)	
	feed interface	coupling (Eq. 7)	
	wall	insulation	
	axis	axial symmetry	
Feed (Maxwell-Stefan convection and diffusion)	inlet	oxygen mass fraction	0.233
	outlet	convective flow	
	axis	axial symmetry	
	membrane interface	coupling (Eq. 7)	
	wall	insulation	
	stagnant zone	insulation	

[1]The values shown are for the reference case

Table 5. Mathematical description of the coupled boundary conditions

Mass flux of oxygen in feed compartment (z-component):

$$J'_{O2} = \rho\, w_{O2}\, u_z - \rho\, w_{O2}\left(\tilde{D}_{O2,O2} - \tilde{D}_{O2,N2}\right)\left(\frac{\partial x_{O2}}{\partial z} + \left(x_{O2} - w_{O2}\right)\frac{1}{P}\frac{\partial p}{\partial z}\right)$$

Molar flux of oxygen in sweep gas compartment (z-component):

$$J_{O2} = -D_{O2,Ar}\frac{\partial c_{O2}}{\partial z} + u_z\, c_{O2}$$

Void diffusion in membrane:

$$J_{Vo} = -D_{Vo}\frac{\partial c_{Vo}}{\partial z}$$

Boundary condition at sweep-gas – membrane interface (z = z_{12})

$$J_{O2}\big|_{z_{1,2}} = -2 \cdot J_{Vo,m}\big|_{z_{1,2}}$$

Boundary condition at feed – membrane interface (z = z_{23})

$$J'_{O2}\big|_{z_{2,3}} = -2 \cdot M_{O2} \cdot J_{Vo}\big|_{z_{2,3}}$$
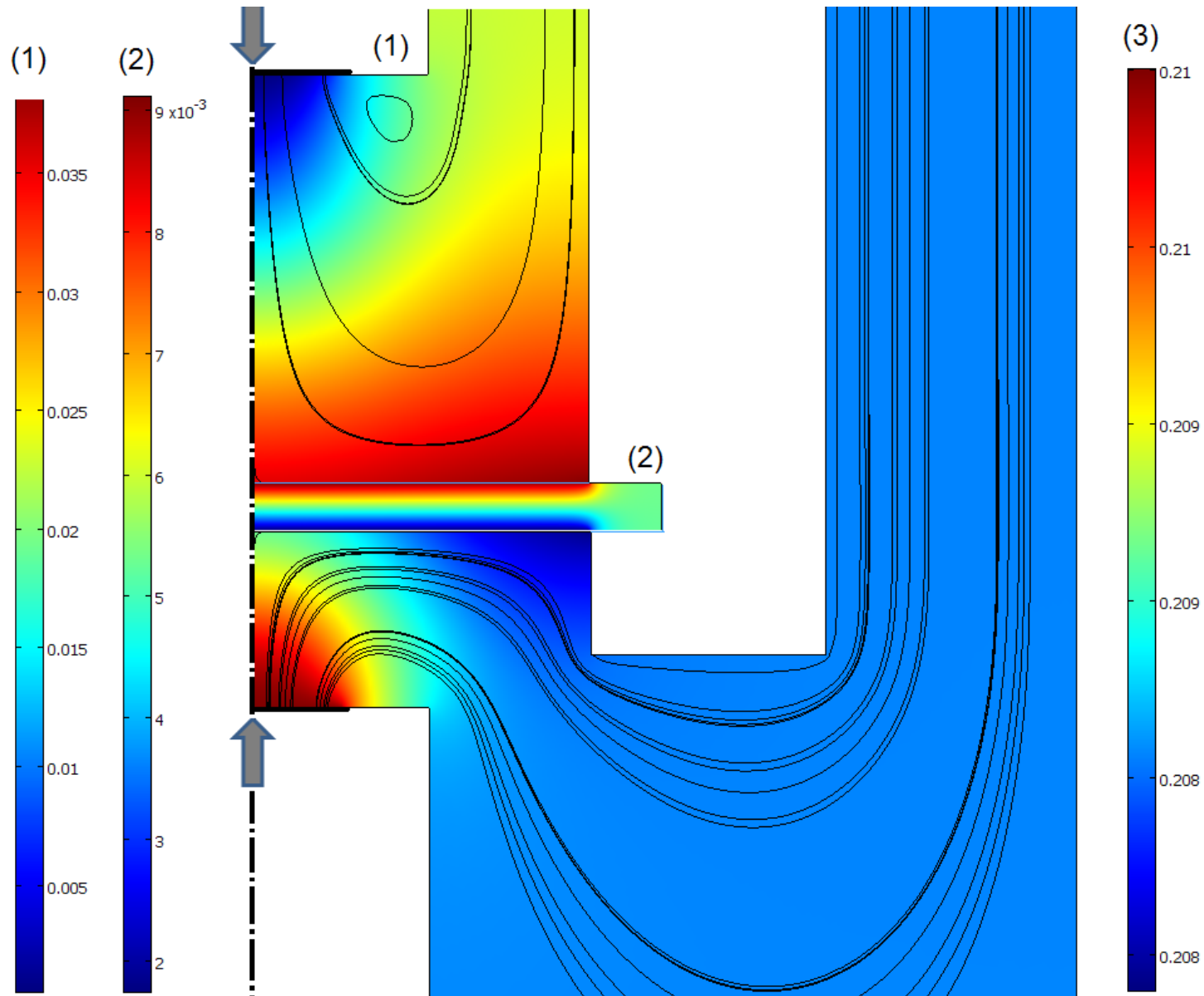
Manuscript with MARKED changes

Supporting Information

From "***Fluid Dynamic Modeling of Oxygen Permeation through Mixed Ionic-Electronic Conducting Membranes***"

by J.M. Gozálvez-Zafrilla, A. Santafé-Moros, S. Escolástico, J.M. Serra*

Figure S1: Mapping of the oxygen partial pressure (atm) in the volume of the permeate (1) and air (3) compartment; and oxygen vacancy concentration (mol·m^{-3}) in the ceramic membrane (2). Scale bars are different for each considered zone. The geometry and operating conditions corresponds to the **reference case** (See Table 1).
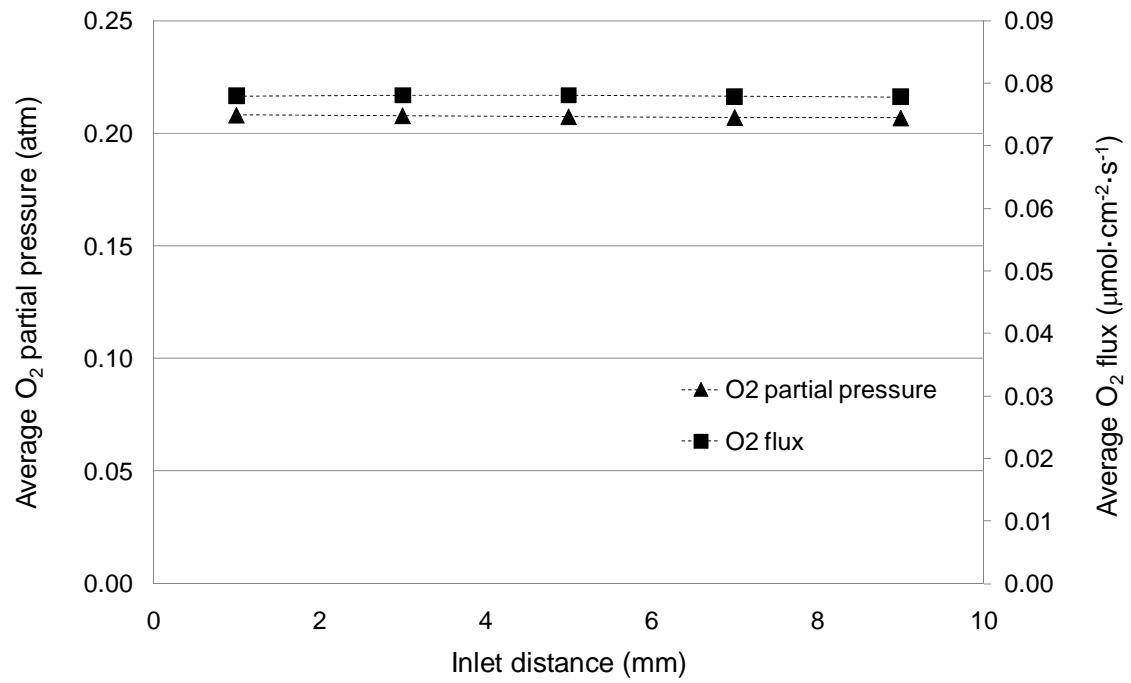
Figure S2: Average oxygen partial pressure on the membrane surface and average oxygen flux (permeation flux) of the feed side as a function of the inlet distance to membrane (r = 1.5 mm).
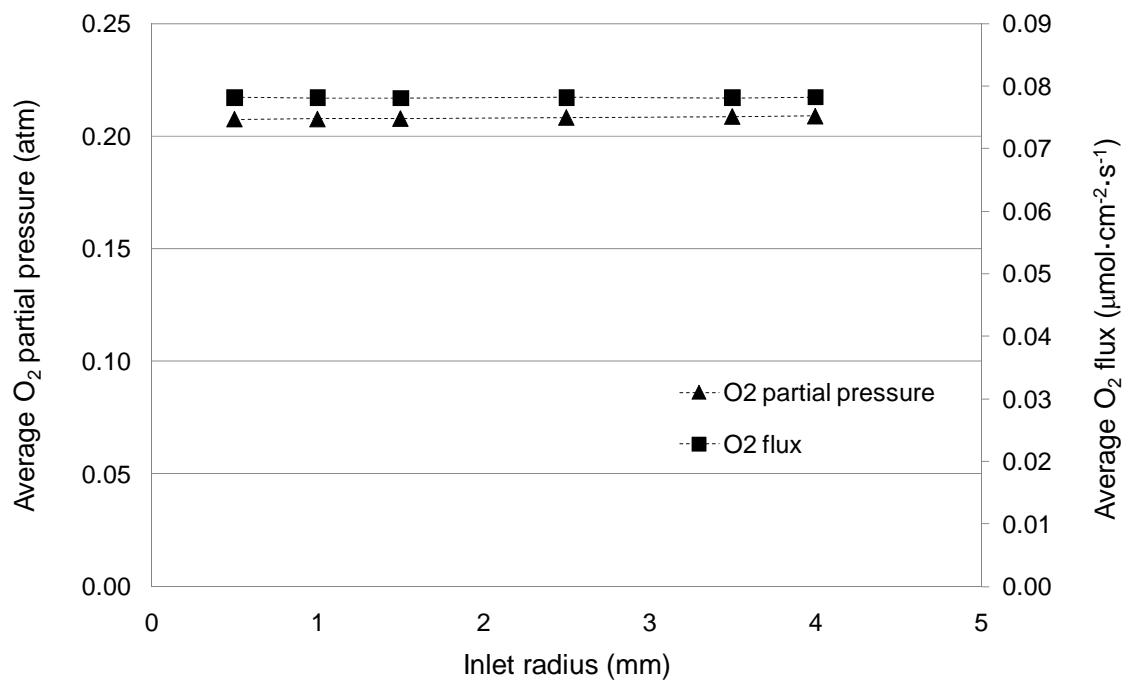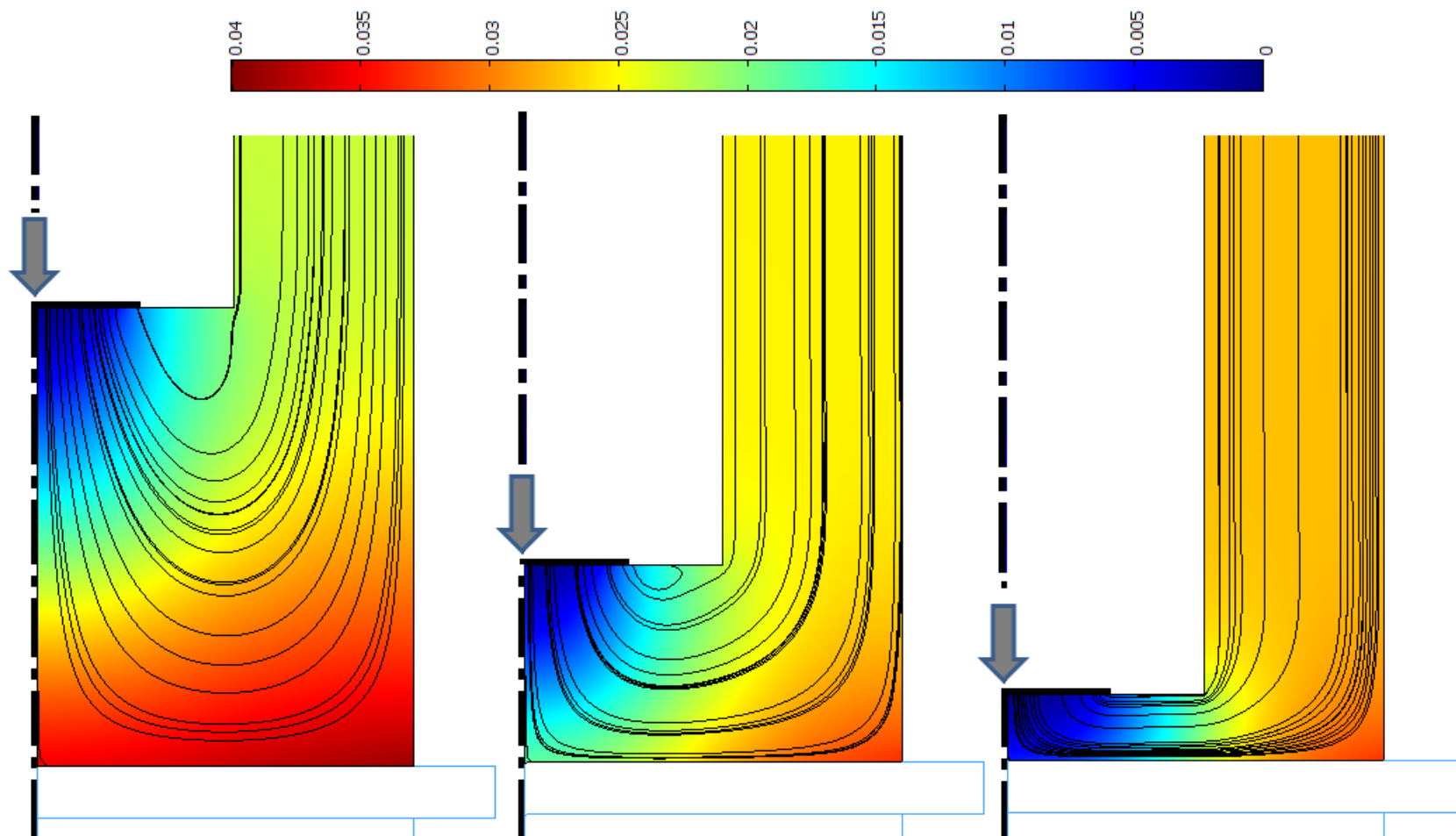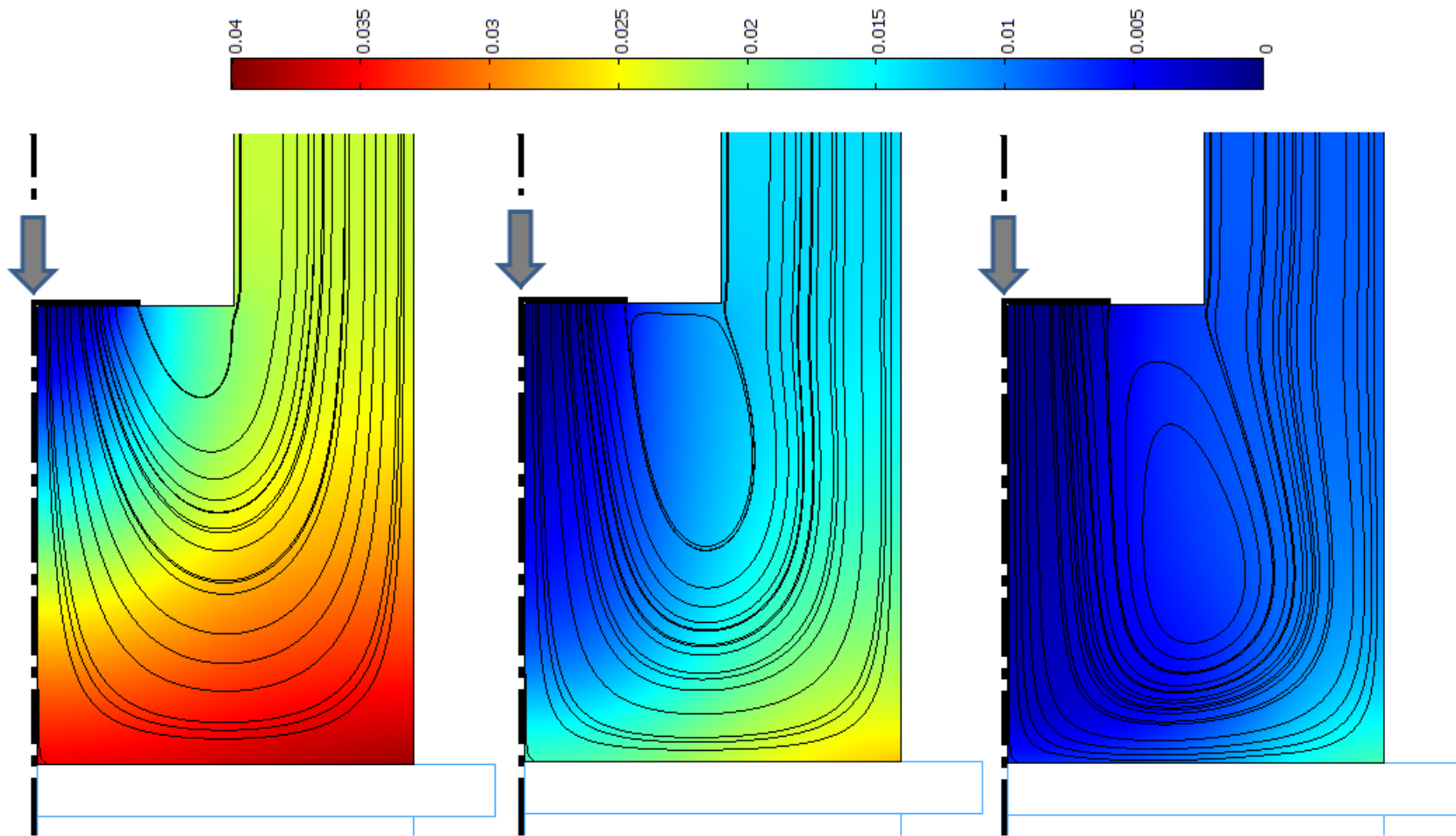
Figure S3: Average oxygen partial pressure on the membrane surface and average oxygen flux of the feed side as a function of the inlet radius (z = 3 mm).

Figure S4: Effect of the variation of the distance between the sweep-gas inlet tube and the membrane surface on the oxygen polarization. Mapping of the oxygen partial pressure (atm) in the volume of the permeate compartment for three different distances (from left to right), Z = {5, 3, 1} in mm. The rest of geometric parameters and operating conditions correspond to the **reference case** (See Table 1).

Figure S5: *Effect of the variation of sweep-gas flow rate on the oxygen polarization. Mapping of the oxygen partial pressure (atm) in the volume of the permeate compartment for three different flow rates (from left to right), Q = {50, 100, 200} in cm^3 (STP)/min. The geometry and the rest of operating conditions correspond to the* **reference case**.

Figure S6: Evolution of the relative error in oxygen balance for the entire rig as a function of the number of elements of the mesh used for the reference case
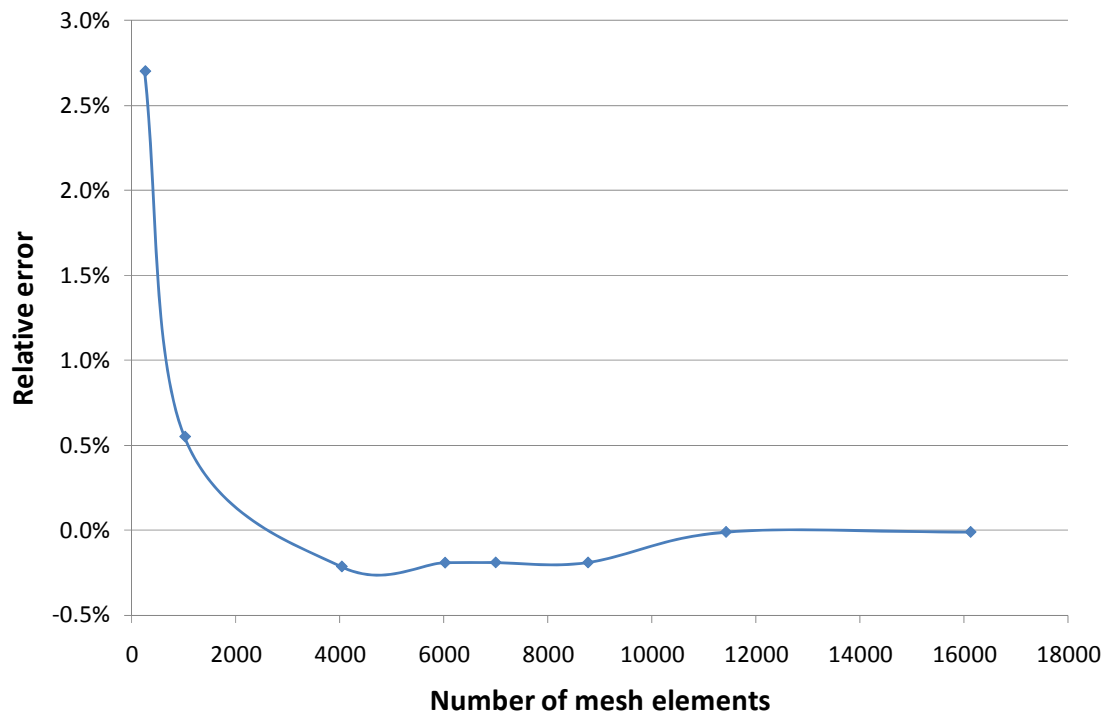
Figure S7. Relative error of oxygen concentration obtained for different mesh sizes with respect to the results obtained for a highly refined mesh (34481 elements). These calculations were performed in a section located one millimeter above the membrane for the base case.
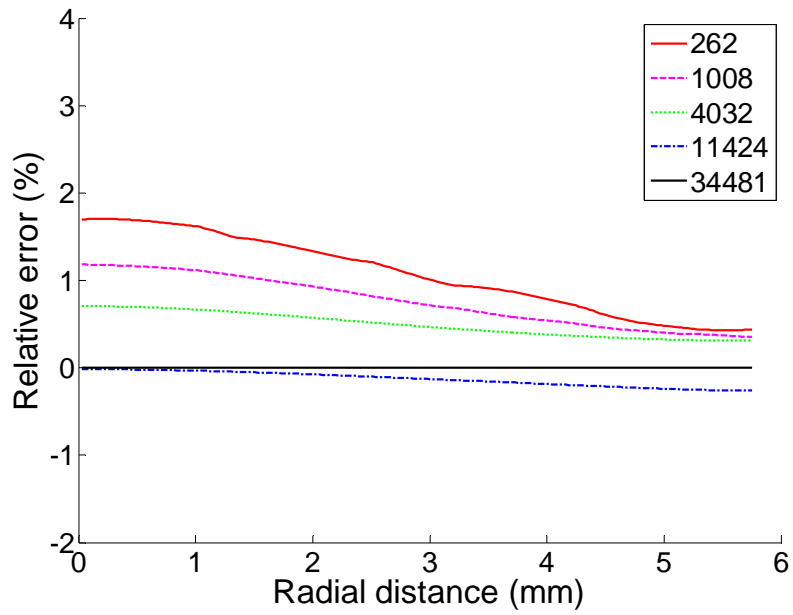
Table S1. Relative errors of oxygen mass balance corresponding to different mesh sizes (coarse mesh : 250-300 elements, medium: 1000-1100 elements, fine: 9500-11000 elements) for some geometries

Z-distance (mm)	Mesh	Inlet radius (mm)	
		0.5	4.0
1	coarse	3.09%	3.57%
	medium	0.34%	-0.17%
	fine	-0.03%	-0.05%
9	coarse	3.04%	3.72%
	medium	0.03%	-0.01%
	fine	-0.03%	-0.02%